UNIVERSITÉ DE GENÈVE
FACULTÉ DES SCIENCES

University of Geneva

Master Thesis

Upgrade and improvements on the FEI4 Telescope

Author:
Nicolas Terrasson

Supervisors:
Pr. Giuseppe Iacobucci
Dr. Mathieu Benoît
Dr. Moritz Kiehn

28 february 2017

Acknowledgements

I would first like to express my gratitude to Prof. Giuseppe Iacobucci for granting me the opportunity of participating and learning in this fascinating collaboration. His advice and support made this work possible.

I would also like to thank Dr. Mathieu Benoît and Dr. Moritz Kiehn for sharing with me their invaluable expertise, knowledge and guidance.

Furthermore, my thanks go to Francesco Di Bello and Branislav Ristic for their precious explanations and help in different parts of this work.

Finally, my gratitude goes to my parents, who never fail to push me ever further.

Contents

I. Introduction

After 15 years of operation, the CERN Large Hadron Collider will be upgraded to a higher luminosity. The HL-LHC project is foreseen to be implemented around 2025. Consequently, new constraints and requirements necessitate the upgrade the experiments in the LHC. The planned long shutdown of 2024 gives the possibility to implement the new hardware.

Because of radiation damage and occupancy saturation, the current Inner Detector of the multi-purpose ATLAS experiment will not be able to fully take advantage of the HL-LHC upgrade. It will be necessary to implement a new particle tracker capable of operating in these conditions. One of the proposed solution is based on commercially available High-Voltage CMOS (HV-CMOS) model of sensors.

These particle trackers are studied in testbeams with the help of the Geneva FEI4 Telescope. To ensure the quality of these analysis, the telescope will be upgraded with the high-resolution Mimosa26 reference planes, already in use in the EUDET telescope [1].

In this study, simulations have been conducted to observe and quantify the impact of the new sensors on the operation of the FEI4 telescope. A modal analysis has also been conducted to study the influence of mechanical resonance on the accuracy of the telescope.

In chapter 1, the LHC and the ATLAS experiment will be shortly described. Chapter 2 will expand on semiconductor detectors theory. In chapter 3, the technology and hardware used in the FEI4 telescope will be discussed. The simulation method and results will be presented in the chapter 4, while the modal analysis methods and results will be described in chapter 5. Finally, the study will be summarized in the chapter 6.

1. CERN

Established in 1954 on the Franco-swiss border near Geneva, the European Organization for Nuclear Research (commonly referred to as CERN) is an international particle physics laboratory, spanning 23 member states and various international collaborations.

1.1 The LHC

Since September 2008, the CERN houses the largest and most powerful (as of 2016) particle accelerator in the world. The Large Hadron Collider (LHC) is the latest addition to the CERN's Accelerator Complex. Its purpose is to make possible the study of high energy interactions to advance understanding of fundamental physics. To this end, it accelerates and collides bunches of protons; as of 2015, the recorded center-of-mass energy was 13 TeV, a world record.

To bring them at the required energy levels, the protons are processed through an accelerating chain of systems, dubbed the Accelerator Complex.

The process starts with a bottle of hydrogen gas. An electric field is applied on the atoms to strip them of their electrons and isolate the protons, which are then brought into the LINAC2. This linear accelerator will bring them to 50 MeV before injecting the beam into the Proton Synchrotron Booster (PSB). When the protons get to 1.4 GeV, they go into the Proton Synchrotron (PS), where they'll go up to 25 GeV. The Super Proton Synchrotron (SPS) accelerates them further to 450 GeV. At this energy level, the beam is ready for injection into the LHC. At every step of this process, various experiments, detectors and secondary beams are placed (for instance, the SPS North Area, where the FEI4 telescope is usually located), as shown on figure 1.

The LHC is a 27 km long underground system, buried 50 to 175 meters deep depending on the location. It can contain up to 2808 bunches, each one 25 ns in front of the other and containing around 10^{11} protons. The beam is accelerated by radio-frequency cavities (RF cavities) and controlled by 6700 superconducting magnets (1232 dipoles for trajectory control, 392 quadrupoles for focusing and higher order magnets for beam correction close to the interaction points). More technical details are available in [3].

The LHC is a collider, meaning that it uses two beamlines (or beam pipes) going in opposite directions and meeting at defined interaction points (IP). This effectively doubles the center-of-mass energy during the bunch interaction (the LHC accelerates each bunch to 6.5 TeV, so that the maximal energy achieved is 13 TeV). The LHC has four collision locations, each one housing an experiment: ALICE, LHCb, CMS and ATLAS (three additional smaller, specialized experiments are also using the LHC beam: TOTEM, MoEDAL and LHCf).

ALICE studies quark-gluon plasma through heavy-ion collisions (lead ions), while LHCb investigates the CP violation processes. Finally, CMS and ATLAS are two general purpose detectors looking for new physics happening when TeV levels are attained (Higgs boson hunting, electroweak symmetry breaking...).

1.2 The ATLAS Collaboration

ATLAS (A Toroidal LHC ApparatuS) is a multipurpose particle detector aiming to probe beyond-the-standard-model physics. To study as many dif-

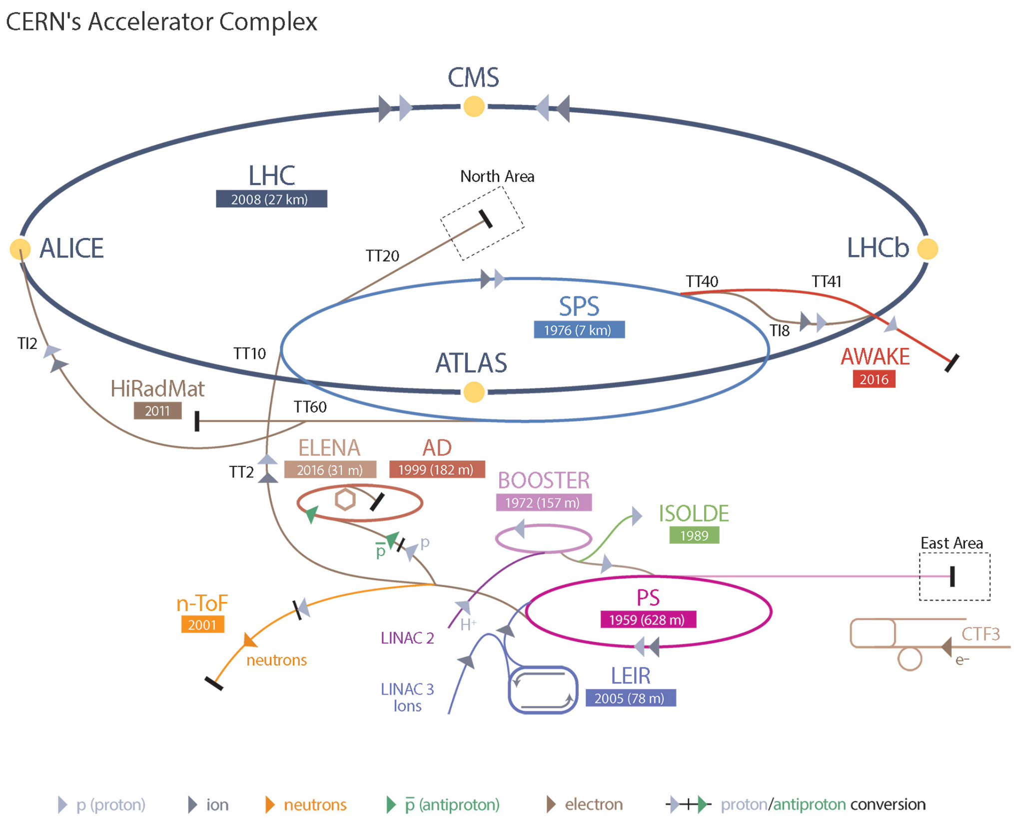

Figure 1: The CERN Accelerator Complex [2]

ferent types of physics as possible, it is equipped with several layers of detectors and devices, with a width of 44 m, a diameter of 22 m, and weighting at 7000 tonnes.

The ATLAS experiment can detect all already established stable particles, except for neutrinos. Their presence is inferred through detection of an imbalance in the momentum of all detected particles. However, for this process to achievable, the experiment must detect all the particles produced at the interaction point (IP). To this end, ATLAS is structured like a barrel around the beam axis and closed by two end-caps, enclosing the IP to ensure optimal hermeticity of the detector.

The Inner Detector is the innermost part of ATLAS. Its purpose is to track particles, giving information about their charge and momentum. To this end, it is surrounded by a solenoidal 2T magnetic field, deflecting the charged particles. After tracking, the curvature of the trajectory allows momentum measurements. The Inner Detector itself is composed of the silicon Pixel

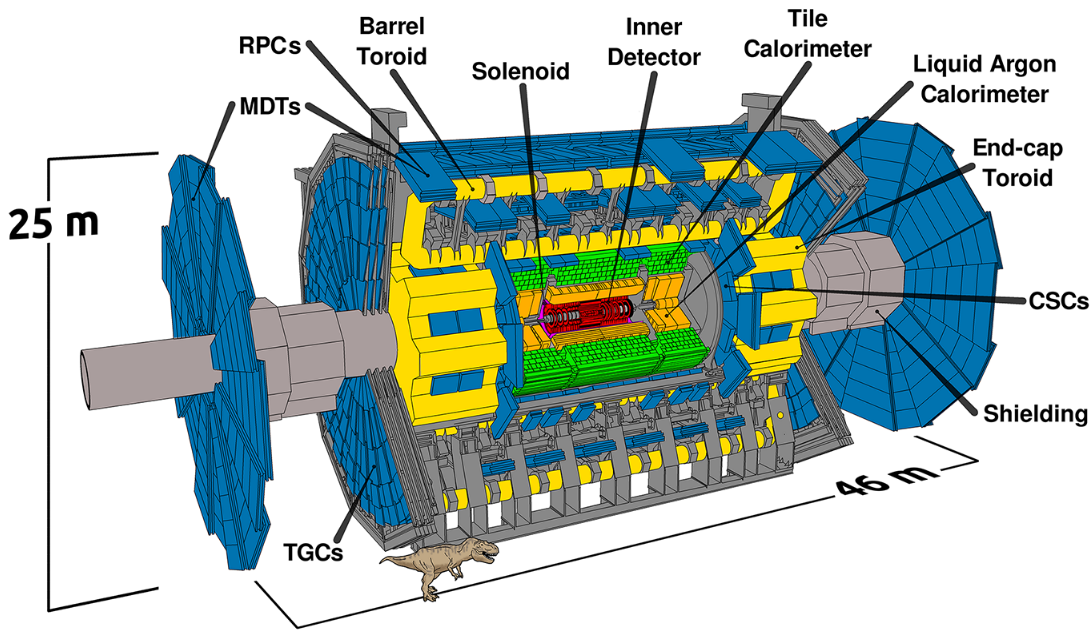

Figure 2: Computer cut-away of the ATLAS experiment. MDT: Muon Drift Tube, RPC: Resistive Plate Chamber, TGC: Thin Gap Chamber, CSC: Cathode Strip Chamber [4]

Detector, the Semi-Conductor Tracker (SCT) and the Transition Radiation Tracker (TRT).

The calorimeter system is placed outside of the inner magnet system. It consists of two devices: the inner electromagnetic calorimeter (ECAL) for energy measurements of electrons and photons, and the outer hadronic tile calorimeter (HTL or TileCal) for energy measurements of neutral and charged hadrons.

The Muon Spectrometer is the last detector in the chain. Immersed in a toroidal magnetic field (2-8T), its purpose is to detect and identify outgoing muons. This sub-detector presents logistic difficulties, but is necessary to ensure complete energy collection (and hence, full hermeticity) inside ATLAS.

1.3 Inner Detector

The inner detector can reconstruct tracks in the pseudorapidity range $|\eta| \leq 2.5$.

Closest to the IP, the Pixel Detector covers radial distances between 50.5mm and 150mm. It is divided into 1744 silicon pixel modules arranged in a three-layered barrel and two end-caps (three-layered disks). Each module

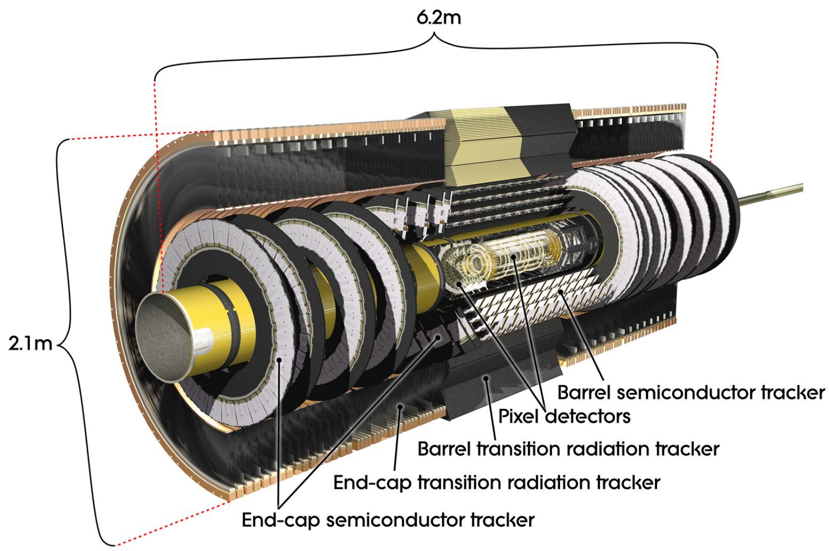

Figure 3: The ATLAS Inner Detector [5]

contains 47'232 pixels for an active area of 16.4mm x 60.8mm.

The SCT is active between the radial distances of 299mm and 560mm. It is formed by 4088 modules of silicon-strip detectors placed in a four-layered barrel and two end-caps (nine-layered disks). Most modules are composed of 4 silicon-strip sensors, where two strips on each side are daisy-chained.

Finally, the TRT spans from 563mm to 1066mm. It consists of 298'304 proportional drift tubes, called straws, arranged in three cylindrical layers.

Although they can operate at ambient temperature, the Pixel Detector and the SCT are cooled by a C_3F_8 evaporative system in order to limit radiation damage. The Pixel Detector operates at 0°C, and the SCT at -7°C. The TRT works at room temperature; only its electronics is cooled.

1.4 Magnet system

The superconducting magnet system is necessary to measure the momentum of charged particles going through ATLAS [6, 7]. In total, it has a length of 26 meters and a diameter of 22 meters. Different subsystems combine to ensure optimal coverage of the detectors: a central solenoid, a barrel toroid and two end-cap toroids. They are cooled by a forced flow helium system circulating through aluminum tubes.

The central solenoid provides an axial magnetic field of 2T to the inner trackers while keeping a low thickness. It is maintained at 4K by the cooling system to ensure that it stays below its critical temperature. The barrel toroid provides a radial magnetic field for muon detection in the layered chambers; it comprises 8 coils and several structural components. Finally, to ensure maximum forward bending at the muon chamber level, ATLAS is capped by two toroid magnets. The three toroid magnets are operating at 77K.

1.5 Calorimeter system

Calorimeters are necessary to measure the energy of the particles produced inside ATLAS. Both ECAL and HTL are sampling calorimeters. Sampling calorimeters are built around a layered combination of two materials: an absorber material and an active material. The absorber material is meant to interact with the passing particle to create cascades (showers) of particles. In an electromagnetic calorimeter (like ECAL), these showers are composed of electrons and photons, whereas in hadronic calorimeters (such as HTL), they are formed of hadrons. These showers are then collected in the active material and total energy is measured or reconstructed.

ECAL uses a lead-liquid argon combination, with accordion shaped absorbers and electrodes. It is composed of a barrel closed by two end-caps [8, 9, 10]. The assembly covers a pseudorapidity $|\eta| \leq$3.2 and is used for electron and photon energy collection.

HTL is composed of scintillator-steel layers and is used for energy reconstruction of hadrons, jets, tau-particles and missing transverse energy [11, 12]. It is formed by a long barrel (pseudorapidity $|\eta| \leq$1.0) and two extended barrels (pseudorapidity 0.8$\leq |\eta| \leq$1.7). The light produced by the scintillator material is transmitted by wavelength shifting fibers to photomultipliers (PMT). The PMT signals are sampled every 25ns (bunch timing).

1.6 Muon Spectrometer

The particles passing through the calorimeter system with mean energy loss rates close to the minimum are called minimum ionizing particles (mip) [14]. In ATLAS, these are muons, and as stated above, the Muon Spectrometer is necessary to measure them and ensure that all particle types are observed. It is composed of several types of chambers placed at different positions in the barrel (three cylindrical layers) or on the end-cap wheels [15, 16].

These chambers work by using wires and/or plates to apply an electrical field to a volume of gas. When a charged particle passes through the chambers, it ionizes the gas and the resulting electrons are collected by electrodes.

In the barrel, Resistive Plate Chambers (RPC) are filling the role of fast-response detectors. Each chamber is composed of two gas volumes, four

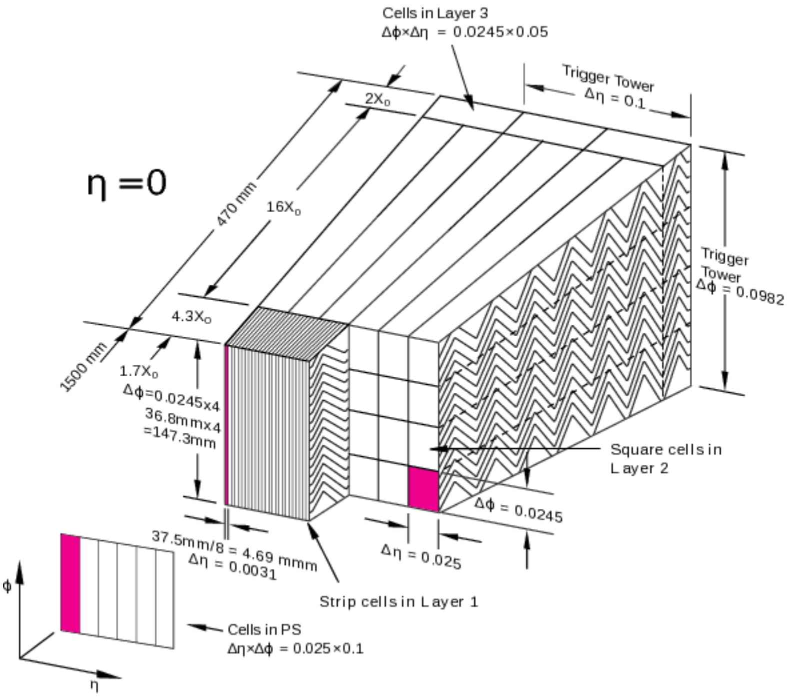

Figure 4: Sketch of an ECAL module. Note the accordion structure of the layers. [13]

planes of read-out strips and bakelite plates, and is operated in avalanche mode. There are three layers of chambers on the barrel, providing triggers for low and high p_T. In the end-cap, the fast-response detectors are the Thin Gap Chambers (TGC). They are composed of multiple wires operated in saturated mode. Put together, the RPC and TGC are the trigger chambers of the Muon Spectrometer.

To measure with more accuracy the muon momentum, precision chambers are used. The main tools for this are the Monitored Drift Tubes (MDT), drift chambers formed with aluminum tubes. They are placed everywhere in the Muon Spectrometer except in the inner part of the end-cap ($2 \leq |\eta| \leq 2.7$). In this area, higher granularity is required because of the background rate. To this end, multi-wire proportional chambers (MWPC) are used, the Cathode Strip Chambers (CSP).

1.7 IBL

The IBL is a fourth pixel layer added inside the ATLAS Inner Detector during the LHC 2013-14 technical shutdown. It is set between the beam pipe and the B-layer. Its design revolves around several important points [18, 19].

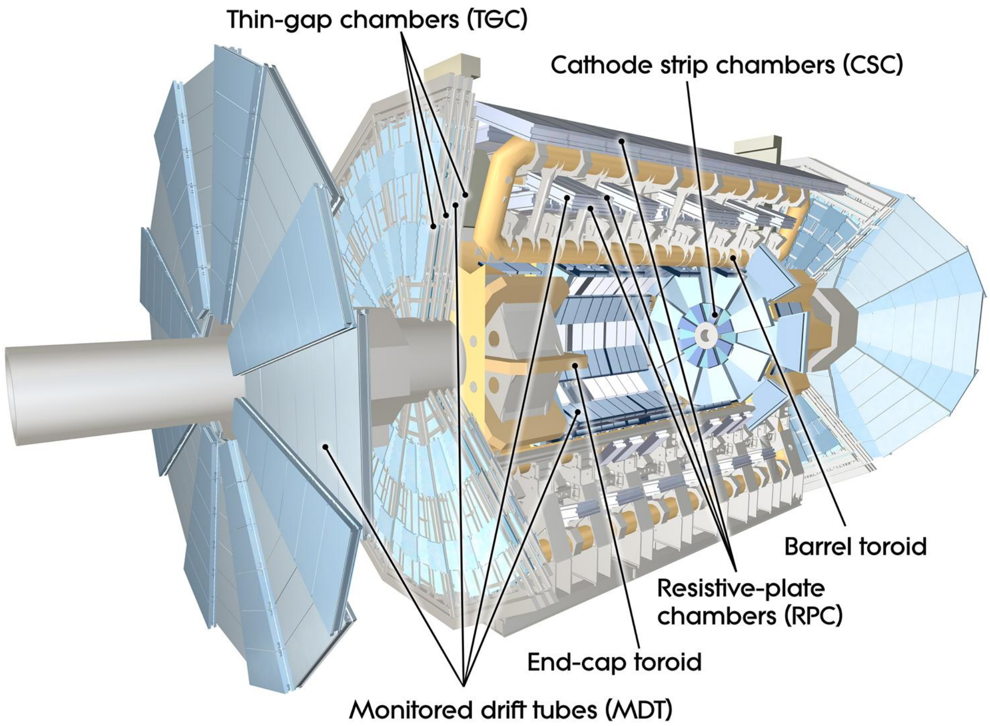

Figure 5: Layout of the ATLAS Muon Spectrometer. The four types of chambers and their respective positions are highlighted, as well as the three supraconductive toroid magnets. [17]

The close proximity to the beam means that the technology used has to be able to operate under radiation-heavy conditions, with radiation hard electronics and sensors. Moreover, the high luminosity increases occupancy, leading to an increased fake rate of tracks: large event pileups mean that clusters can combine randomly, especially inside the B-layer. This would notably lead to a lower b tagging efficiency. The addition of the IBL means a higher redundancy and a reduced fake rate.

Additionally, tight mechanical constraints inside ATLAS mean that complex engineering processes are necessary to accommodate the requirements.

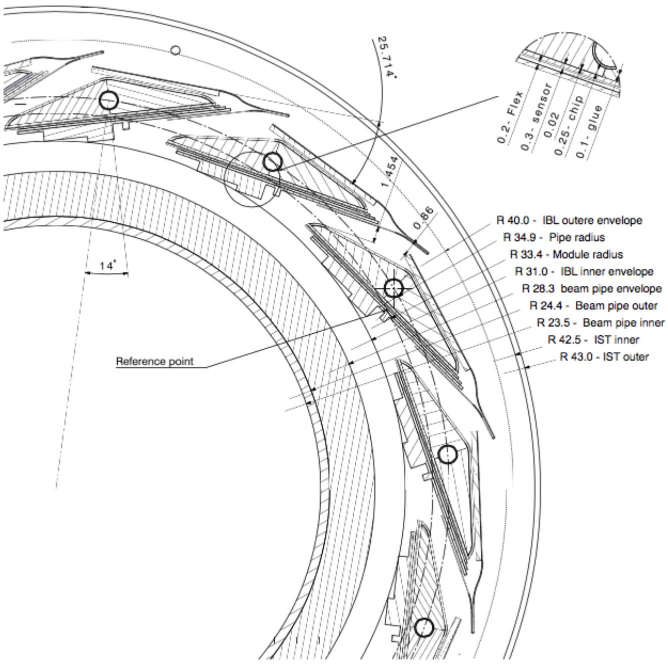

Figure 6: Schematics of the IBL pixel layer [20]

II. Theory

1. Semiconductor properties

1.1 Why use semiconductor detectors?

The *semiconductor diode detectors*, also called *solid-state detectors*, bear a number of advantage over gas-filled and scintillation detectors, making them a valuable asset for radiation detection. Notably, the typical higher density of a solid medium compared to a gas medium make them much more practical and compact for the measurement of high energy particles. The high number of charge carriers produced in a semiconductor diode detector ensures good energy resolution; coupled with their relatively fast timing characteristics and compact size, this makes them a good complement to photomultiplier detectors, depending on the needs of the experiment.

The drawbacks inherent to the semiconductor detectors are a limitation the limited sizes of active area, high sensibility to radiation-induced damages and the need for cooling systems. These arise notably from the rather high level of noise produced. The most used materials for these detectors are silicon and the germanium. Lately, there is also research and development toward the use of diamond detectors, although they are still not widely used.

1.2 Band structure and charge carriers

In crystalline materials, the disposition in periodic lattices imposes energy bands for the electrons inside the crystal. This means that an electron must be confined in one of these energy bands and is not allowed to be in a energy state, called gap, between these bands. The lower energy level band is called the *valence band*; it corresponds to the energy level of the electrons confined to the outer shell of the atoms forming the crystal. These electrons are bound to specific sites in the lattice [21]. For instance, in the silicon and the germanium, they are part of the covalent bond maintaining the structure. The higher energy level band is called the *conduction band*. The electrons at this energy level are free to migrate through the material and contribute to the electrical conductivity of the crystal.

These two bands are separated by a *band gap*, the size of which determines the type of material: insulator, semiconductor or conductor. If the bandgap is relatively big (typically, more than 5 eV), it is an insulator. The electrons would need a lot of energy to go the conduction band, and therefore, these materials have a very bad conductivity. If the bandgap is smaller than that, it is then a semiconductor. Finally, if the bands are overlapping, it is a conductor. In this case, the electrons can easily move between the valence and conduction bands; this is typically the case with metals.

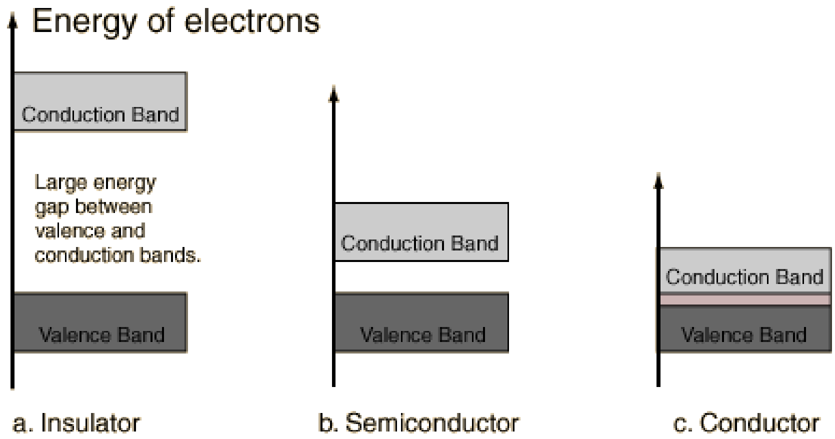

Figure 7: Band structure for different types of material. [22]

The number of available sites in the valence band of semiconductor and insulator corresponds exactly to the number of electrons in the pure material. Without any thermal excitation or external addition of energy, the electrons are all confined in the valence band, and the conduction band is empty. Therefore, at a zero temperature, the semiconductor and insulator materials should theoretically not show any electrical conductivity.

When the temperature is higher than zero, some thermal energy is added in the system. An electron can then absorb enough energy to cross the gap between the valence and conduction band. This represents an electron freeing itself of its orbital and drifting in the crystal. This leads to the creation of a negative charge in the conduction band, but also to a vacancy in the valence band, which can be seen as a positive charge called a *hole*. The whole process leads then to the creation of an *electron-hole pair*. The probability for the creation of an electron-hole pair is highly dependent on the ratio between the bandgap energy and the absolute temperature.

In these circumstances, the pair would finally recombine, establishing an equilibrium. But if an electric field is applied, the electrons and the holes created would undergo a net migration. The application of the field on the charge carriers creates a *drift velocity*; the holes move along the direction of the electric field, and the electrons in the opposite direction. For moderate values of the field, the drift velocity is directly proportional to its intensity. At higher values, the carriers reach the *saturation velocity*. The combination between a high saturation velocity and small size detectors explains the short response time typical of semiconductor detectors.

1.3 Intrinsic semiconductor

In a semiconductor, the number of electrons in the conduction band corresponds perfectly to the number of holes in the valence band. In this case, it is called an *intrinsic semiconductor* and its properties can be described. However, in practice, it is impossible to obtain a perfectly pure semiconductor, even with silicium and germanium, that can reach high level of purity.

We take n the concentration of electrons in the conduction band and p the concentration of holes in the valence band, known as *intrinsic carrier densities*. Then, for an intrinsic semiconductor:

$$n_i = p_i \tag{1}$$

These densities are proportional to the ratio of the absolute temperature over the bandgap energy.

1.4 Doping

It is possible to adjust the properties of the semiconductor material by intentionally adding a small amount of impurities, a process called doping. To observe the effect of doping on a semiconductor, we consider a silicon crystal. Silicon is a tetravalent element, so it forms covalent bonds in the crystal; all the sites in the valence band are occupied. If pentavalent impurities are added, they will take the place of silicon atoms within the lattice and provide additional electrons lightly bound to their sites. Since they have energy levels near the gap top, they can occupy the forbidden gap, which means that they can move in the conduction band with relatively small thermal excitation. Therefore, the electron density in the conduction band is totally dominated by the impurity contribution:

$$n \cong N_D \tag{2}$$

These impurities are known as *donor impurities*. The higher concentration of electrons shifts the recombination equilibrium. The number of holes has then to decrease, so that the product of n and p stays the same as for the intrinsic values:

$$np = n_i p_i \tag{3}$$

These type of doping is referred to as *n-doped*. In a n-type semiconductor, the electrical conductivity is much higher and dominated by the electrons, with respect to the intrinsic semiconductor. This is why, in this case, the electrons are called *majority carriers* and the holes *minority carriers*.

Now, if the added impurities are trivalent, they become *acceptor impurities*, since they leave unsaturated covalent bonds. These electron vacancies are similar to holes, although with slightly different properties. Electrons bound to these sites are slightly less fixed than normal valence electrons, so that they occupy an energy level in the forbidden gap, but this time, near its bottom. This means that the valence electrons need only a small amount of thermal energy to occupy this state, leaving holes in the valence band. Since there is approximately one extra hole created in the valence band for each acceptor impurity, the total number of holes is dominated by the concentration of acceptors:

$$p \cong N_A \tag{4}$$

The equilibrium between electrons and holes is still maintained by equation (3). This time, the holes are the majority carriers and the electrons the minority carriers. The semiconductor is said to be *p-doped*, and its electrical conductivity is higher than for an intrinsic semiconductor.

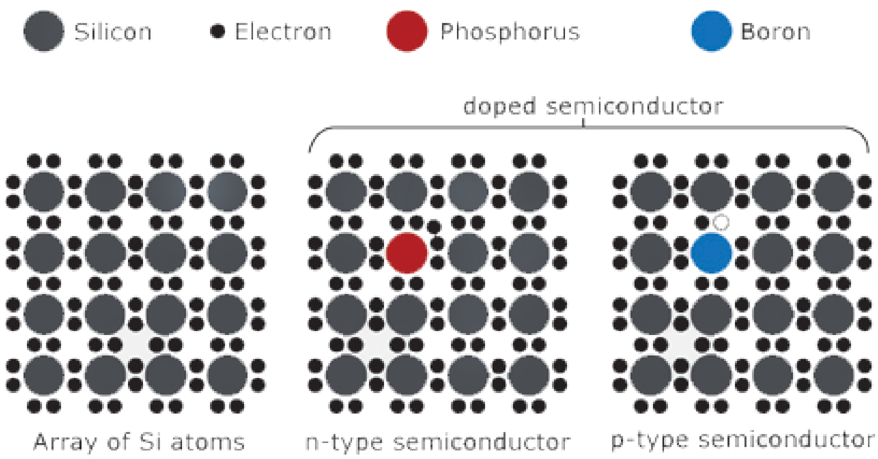

Figure 8: Effect of doping impurities in a silicon crystal. [23]

Finally, if both donor and acceptor impurities are added in equal concentration, the material is called *compensated*. Theoretically, its properties are close to the intrinsic ones, but in practice, it is impossible to achieve perfect compensation, and a slight imbalance is enough to turn the material into a n-type or p-type semiconductor.

Sometimes, a thin layer of semiconductor can have a very high concentration of impurities. These heavily doped materials are often designated by n^+ and p^+, and they have consequently a high conductivity. If instead the material is only mildly doped, it can be designated by ν and π [21].

1.5 Trapping

Various impurities and structural defects can affect the motion of the charge carriers, and thus the properties of the detector. Notably, metal impurities introduce energy levels near the middle of the band gap (*deep impurity*). These impurities trap carriers and release them after a time long enough to prevent their contribution to the pulse. Impurities can also act like *recombination centers*, where annihilation of electron-hole pairs can occur.

When determining the structure and operation of the semiconductor detector, it is necessary to take into account the specifications of the material, such as the average lifetime of the charge carrier and the trapping length: with a short average lifetime and large trap interference, the maximum travel length of the charge carriers is reduced, putting an upper limit to the size of the detector.

1.6 Ionizing radiation

Incoming charged particles going through a semiconductor deposit energy in the medium and create electron-hole pairs. This is the mechanism at the core of the semiconductor radiation detection, so the main relevant quantity for the study of the solid-state detectors is the average energy used by a charged particle to produce an electron-hole pair, called *ionization energy*, or ϵ. Since it has been observed that ϵ is largely independent to the energy of the incident radiation, the number of charge carriers can be used to approximate the deposited energy of the observed particle. The important characteristic of the semiconductors detectors resides in the small value of their ionization energy (a few eV), typically 10 times smaller than in a gas-filled detector (around 3 eV in silicon and germanium, 30 eV in a gas detector), so that for a given energy, there are 10 times more carriers produced [21]. This is especially important for reducing the effect of the statistical fluctuations in the number of carriers, which is often the main limitation on the energy resolution.

If all the events along the ionizing path were totally independent, the whole process would follow a Poisson model, and the variance over the number of produced electron-hole pairs would be the ratio of the total energy over the ionization energy, E/ϵ. The Fano factor F is used to describe the difference between the observed and predicted variance:

$$F \equiv \frac{\text{observed statistical variance}}{E/\epsilon} \tag{5}$$

The Fano factor has to be determined for each experimental setup, to be able to take into account other factors, such as electronic noise. For a good energy resolution, this factor should be as small as possible.

2. Radiation detection

2.1 Current collection

The solid-state detector configurations use applied electric fields, so that when electron and holes are created by a charged particle, they drift in opposite directions until they are collected at the boundary of the active volume. In silicon and germanium, the mobility of the holes is reasonably close to the mobility of the electrons (in silicon at 300K, electron mobility is at 1241.8 $cm^2/v{\cdot}s$, hole mobility at 406.9 $cm^2/v{\cdot}s$ [24]), which means that the two carriers can be collected together.

In order to collect these carriers, electrodes are placed at either boundary of the material. If ohmic contacts are used, positive and negative charges are free to flow through them, so that with two contacts positioned face to face, the charge carrier concentrations are maintained at the equilibrium. However, all semiconductors produce a *leakage current* induced by fluctuations, and with this type of electrodes, the noise level is so high that an ionizing radiation signal wouldn't be observable anymore. This means that *non-injecting* or *blocking* electrodes have to be used, and more specifically, p-n semiconductor junctions. With these solutions, the leakage current is largely reduced, making it possible to detect the signal induced by an ionizing radiation.

2.2 Semiconductor junction

The p-n junction is a semiconductor with a n-type region and a p-type region. The two parts are in contact, thus forming the junction. At this junction, conduction electrons from the n-type region will diffuse into the p-type region, combining with the holes present there. This process leaves a hole (in this case, an ionized donor impurity) in the n-type region. Similarly, holes from the p-type region will combine with the electrons in the n-type region, leaving a fixed electron. The overall effect is that a positive space charge appears in the n side, and conversely, a negative space charge appears in the p side.

In this region, called *depletion region*, an electric field formed by the charge distribution prevents further diffusion of the carriers, through the *contact potential*.

A great property of this depletion region is that its electric field pushes electrons in the n-region and holes in the p-region, effectively suppressing the carrier concentrations. The charges in the depletion region are mainly immobile ionized donors and filled acceptors, which lead to a high resistivity. In the case of incoming ionizing radiation, the created electrons and holes are evacuated from the depletion region by the electric field, forming the basis of an observable signal.

2.3 Reverse biasing

Keeping in mind that the contact potential naturally induced in the depletion region is not strong enough to effectively detect an incoming ionization, an external electric field is applied to the material. The direction in which this field is applied is particularly important. Indeed, the p-n junction possesses a "forward" and a "reverse" direction. If the voltage applied on the p-region is positive with respect to the n-region, it will affect holes from the p-region and conduction electrons from the n-region, which are the majority carriers. This means that a small value of forward bias voltage is enough to produce intense currents.

In the reverse situation, the applied bias affects minority carriers, and the potential difference in the depletion region is enhanced. The p-n junction works then like a filter, letting the current flow more easily in one direction than in the other. However, if the reverse bias is strong enough, it will provoke a sudden breakdown in the diode, producing a reverse current.

The reversed bias has the added effect of extending the depletion region, offering the possibility of creating a *fully depleted* detector by extending the depletion region over the whole active volume. Otherwise, it is known as a *partially depleted* detector. The size of the depletion region is given by:

$$d \cong (\frac{2\epsilon V}{eN})^{1/2} \tag{6}$$

$$d \cong (2\epsilon V \mu \rho_d)^{1/2} \tag{7}$$

ϵ is the dielectric constant of the medium, μ the mobility of the majority carrier, ρ_d the resistivity of the doped semiconductor. To maximize the size of the depletion region for a given applied voltage, a high resistivity is necessary. The resistivity depends notably on the purity of the medium before doping,

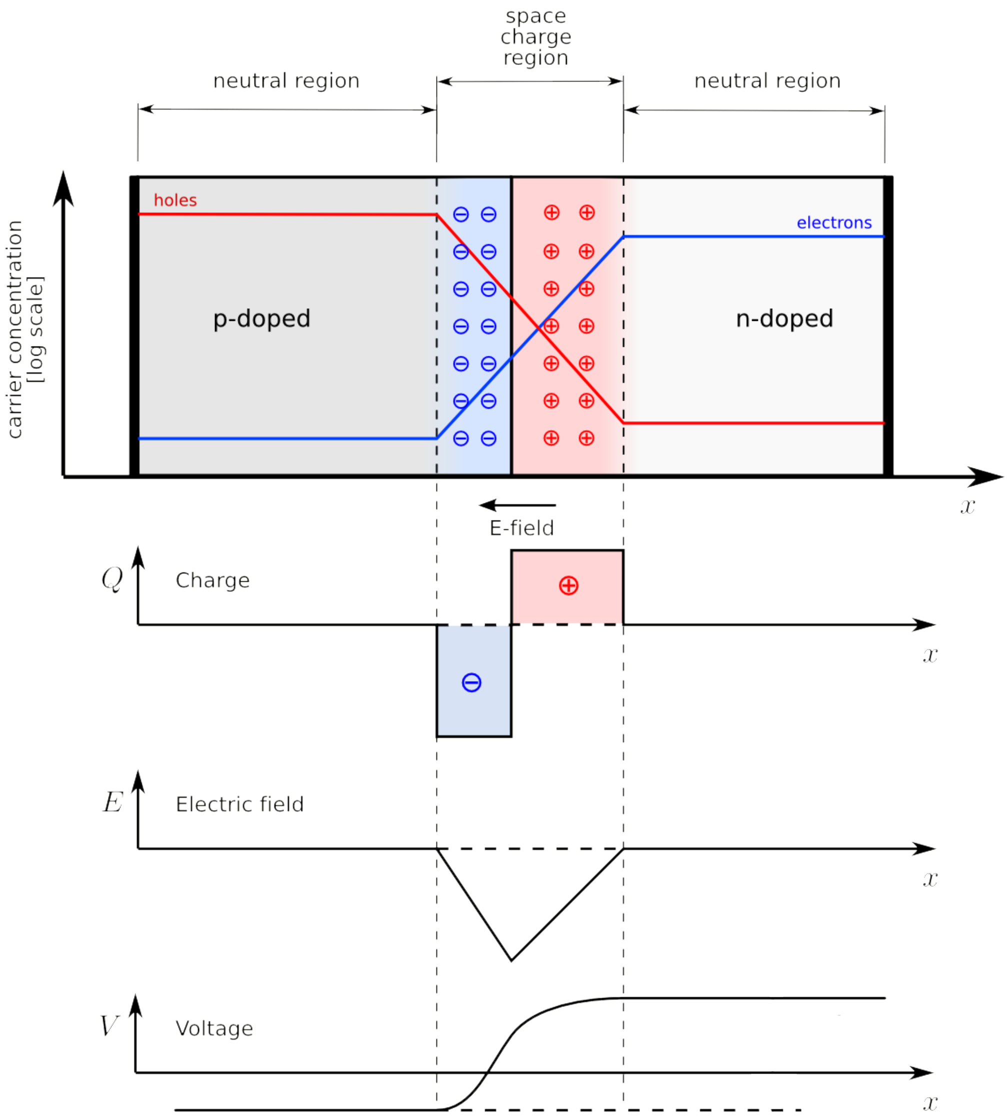

Figure 9: Example of a simple p-n junction as a function, showing the profiles of the charge, electric field and voltage. [25]

so that high levels of purity are required even for the fabrication of doped semiconductors.

3. Semiconductor Detectors

3.1 Depletion configuration

In the early development stage of semiconductor detectors, the p-n junction was created by exposing a p-type material to an n-type impurity vapor. Using this method, it is not possible to obtain a fully depleted material, so this leaves a *dead layer* of inactive material which interferes with the measures (partial depletion). Therefore, the modern detectors are not built anymore with a diffusion method.

The method best suited to the fabrication of a fully depleted detector is by forming a junction with a heavily doped layer on one side and a high-purity, weakly doped (ν or π) semiconductor on the other. When the voltage is applied, equation (7) shows that the depletion region will expand mostly in the high-purity side. This means that the heavily doped region can be made very thin.

Additionally, to get to a state of full depletion, the applied voltage has to be strong enough to extend the depletion region all the way to the back of the wafer. This value is called the *depletion voltage*, and can be found by replacing the size of the depletion region in equation (6) by the thickness of the wafer T:

$$V_d = \frac{eNT^2}{2\epsilon} \tag{8}$$

At this value, there is an electric field throughout the whole wafer. If the applied voltage greatly exceeds the depletion voltage, the electric field will tend to be more uniform everywhere in the detector, which in this case is said to be *over-depleted*.

In practice, the detector is formed first by taking a high-purity ν or π material. A thin layer of a heavily doped semiconductor of the opposite type is then applied on one end of the wafer to act as the *rectifying contact*. It also acts as a blocking contact. On the other end of the high-purity material, though, the minority carriers are free to move, so another blocking contact (heavily doped semiconductor) is added to reduce the leakage current. This blocking contact is of the same type as the wafer, so that it does not create a new depletion region.

To get the best energy resolution for the fully depleted detectors and avoid energy loss variations, it is important that the windows of dead layers (rectifying and blocking contacts) be as small as possible. The wafer should also have the most uniform thickness possible.

3.2 Leakage current

An important electric characteristic of a semiconductor detector is its leakage current. With the use of a blocking contact, it can be greatly reduced. Still, a steady leakage current remains. It is produced in the volume of the detector (*bulk* leakage current) or at the edges of the junction (*surface* leakage current). The bulk leakage current is produced by the combination of the minority carrier current, although very small, and the thermal generation of electron-hole pairs. Typically, silicon detectors can be used at room temperature, but the germanium detectors, having a smaller band gap, have to be cooled to be effective because of this thermal current. The surface leakage current is more prone to variations and depends on a variety of factors: production method, surface contamination, humidity, etc.

The leakage current has also the effect of reducing the effective voltage throughout the wafer. The applied voltage has to include a compensation to counteract this loss.

The leakage current is also useful to detect the breakdown voltage of the diode (I-V measures), and can be used to monitor radiation-induced damages or other malfunctions.

The major source of electronic noise in the detector come then from variations in the bulk and surface leakage current, as well as practical sources (resistance noise, bad contacts).

Informations about semiconductor and detector technologies are available in [21, 26, 27].

III. Technology

1. Pixel Detectors

1.1 HV-CMOS

The High Voltage Complementary Metal-Oxide-Semiconductors (HV-CMOS) are used in a wide array of applications, notably in the particle detector domain [28]. The HV-CMOS pixel sensors have a 100% fill-factor, high tolerance to radiation-damage, in-pixel reading capacities and low prices, with potential for good time-resolution and signal-to-noise ratio (SNR) [29]. This makes for ideal tools in large-scale high energy experiments like ATLAS.

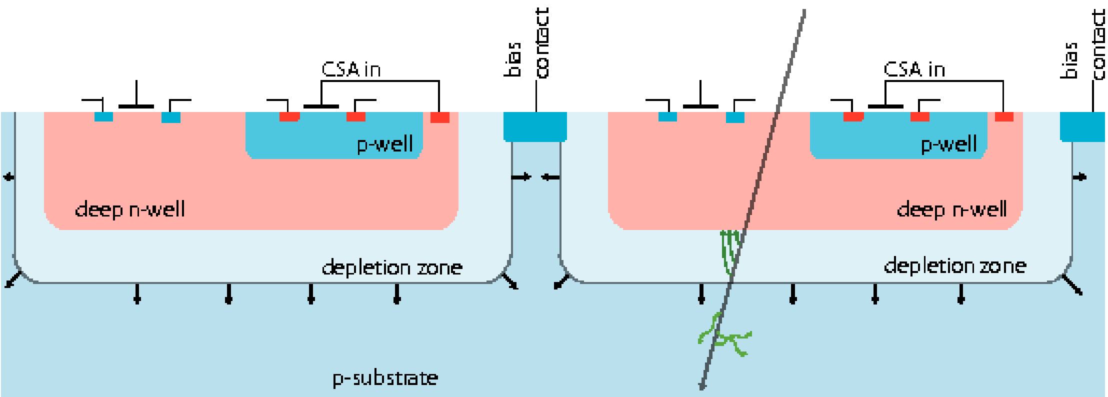

Figure 10: Cross section of a simplified HVCMOS. Note the embedded p-well inside the deep n-well. [30]

The basis of a HV-CMOS detector is a deep n-well placed on a p-type substrate. Inside it is embedded a small p-well, so that the whole area can accept both p- and n-channel transistors (PMOS/NMOS). The n-well is used as a charge-collection electrode and isolates the low-voltage devices from the high-voltage (strong negative bias) p-type substrate, so that the transistors are not damaged. Since it acts as a diode with its own integrated signal processing, it is referred to as a "smart diode"; the whole pixel array is then a "smart diode array" (SDA).

1.2 The FEI4 chip

Conditions inside the IBL put heavy constraints on devices and required the development of new technologies [19]. The Front End-IBL 4 (FEI4) chip was built with these requirements in mind to provide radiation hard, high efficiency read-out electronics.

A single FEI4 integrated circuit (FEI4 IC) consists of an array of 26'880 pixels (80 in the z/beam-direction, 336 in the azimuthal rϕ-direction; see ATLAS detector coordinates), with a pixel size of 250x50 μm^2. Every pixel stores data locally until triggering, an improvement over the FEI3 system of pixel column drain and peripheral data storage. This new matrix architecture allows higher higher efficiency for the FEI4 IC.

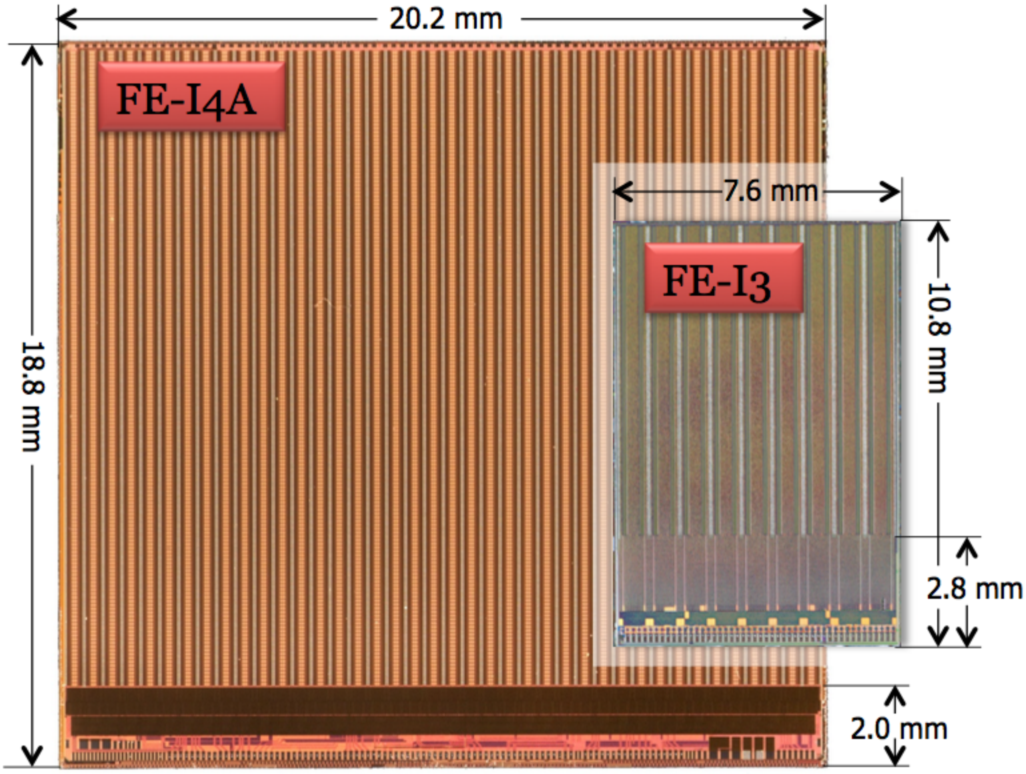

Figure 11: Picture of an FEI4 chip, with an FEI3 for comparison.

1.3 Mimosa26 planes

The MIMOSA (Minimum Ionising Particle MOS Active Pixel Sensor) pixel detectors are a new type of CMOS detectors developed for high precision particle tracking [31]. After several prototypes, the Mimosa26 model became the first large scale sensor of the MIMOSA series. It has been first used in the EUDET telescope project at DESY (Hamburg) [1]. The EUDET telescope project at DESY (Hamburg) required plane detectors with high spatial resolution (uncertainty of 2 μm), large sensitive area (2 cm^2) and high data output capabilities (10'000 readouts/second, 10^6 particles/cm^2/s), which led to the development of the Mimosa26.

Like for the FEI4 IC, a matrix of pixels forms the Mimosa26 plane detector: 663'000 pixels in 1152 columns and 576 rows. Each pixel has an area of 18.4x18.4 μm^2. Rows are read one after another with an 80 MHz clock frequency (the Mimosa26 can be used with a double data output). A single line readout takes 200 ns, leading to a full integration time of 115.3 μs. The detector has an active area of 2.24 cm^2 (21.20 mm x 10.60 mm) for a total size of 2.97 cm^2.

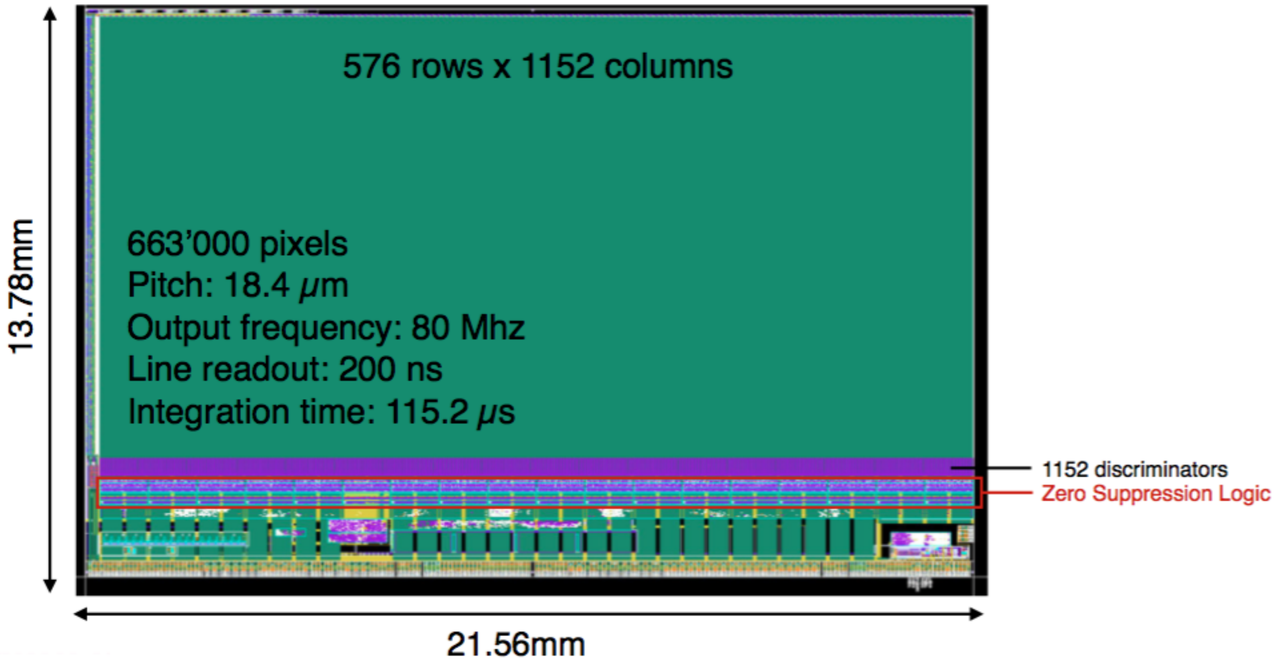

Figure 12: The Mimosa26 plane detector. [32]

The Mimosa26 detector uses a zero suppression logic architecture (SuZe) for data reading. Activated pixels are grouped in each row in a "state" (see fig.6). Each state includes the address of its first pixel and the number of following activated pixels (from 0 to 3).

The whole Mimosa26 is divided in 16 blocks of 64 columns each; every block can store at most 6 states. Moreover, a single row is limited to 9 states per readout. Finally, the limit on a single data output is 570 states per frame. With the double data output (2x80 MHz), the Mimosa26 can then store up to 1140 states per frame.

The SuZe logic improves the readout efficiency of the sensor and enables the detection of dead rows or columns through pattern recognition, because

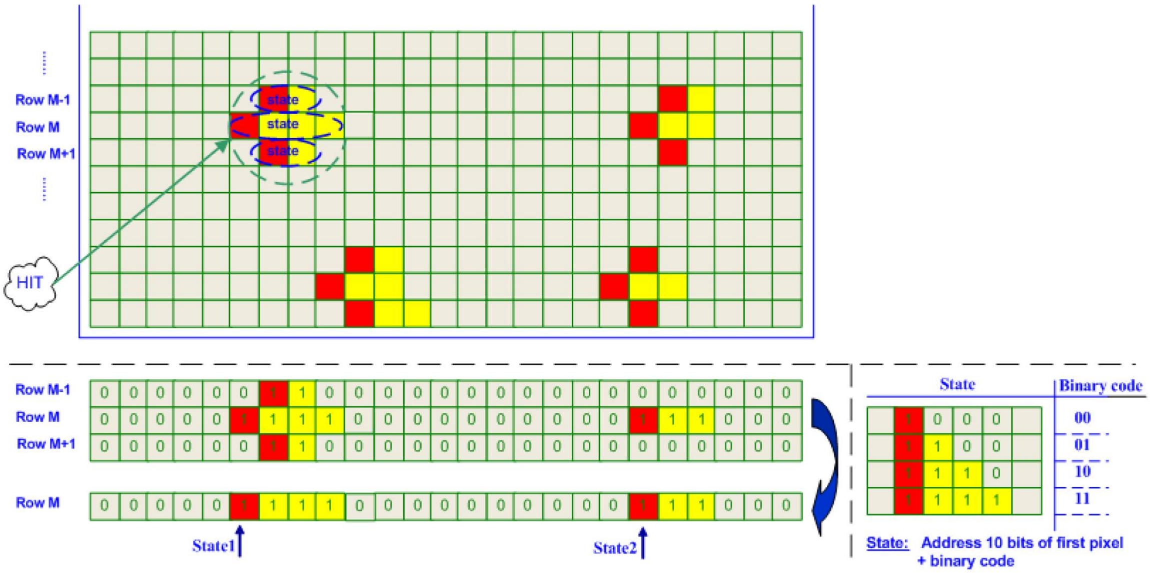

Figure 13: The SuZe logic at the pixel level. [32]

of the memory limitations at the different levels.

Compared to the FEI4 IC, the Mimosa26 detector offers a higher spatial resolution, at the cost of a slower integration time. Thus, it would be best used in combination to take advantage of its specifications.

2. The FEI4 Telescope

Since 2014, the University of Geneva has been using a beam telescope (charged particle tracker) based on the FEI4 chip, dubbed the FEI4 telescope [33]. It is usually located in the SPS test-beam area (H8 beamline, 180 GeV π^+) and used for characterization of various ITK particle tracker models.

2.1 Telescope structure

The telescope is built around an insulated test-box enclosing the Device Under Test (DUT) on a threaded baseplate. The DUT box is injected with cold nitrogen gas to ensure a dry atmosphere and contains a baseplate actively cooled by a silicon-oil chiller, ensuring working conditions for different types of DUTs. The temperature and humidity levels are constantly monitored through sensors placed in several locations. The box is placed on a XY stage to allow for fine positioning of the DUT.

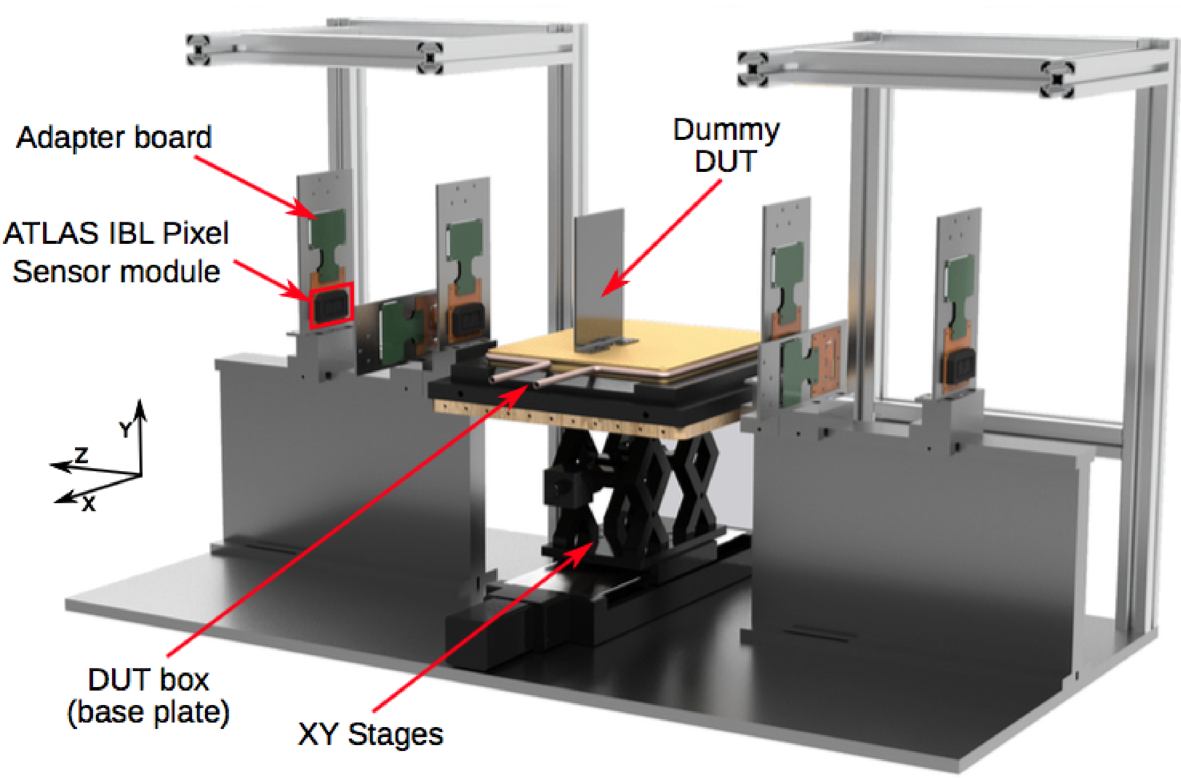

Figure 14: Computer generated image of the Geneva FEI4 telescope.

A new DUT box has been developed and built by the DPNC mechanical group during may 2016, providing improved insulation and ergonomics. A study has been conducted to test its thermal characteristics; it is discussed in the appendix.

Two mechanical arms are placed along the beam axis on each side of the central box; each one holds three FEI4 detector planes. Because of the FEI4 pixel pitch ($50 \times 250 \mu m^2$), the middle planes of each arm (planes n°2 and 5) are tilted to ensure approximately identical spatial resolution on the X and Y axis. The arm planes are working at room temperature and humidity.

2.2 Track reconstruction

The raw data obtained by the FEI4 telescope is processed through several steps by the Proteus (formerly known as Judith) reconstruction framework. This fast, C++ analysis tool handles data in a ROOT file format, while setups and geometry descriptions are encoded in configuration files [34, 35].

The analysis procedure goes as follow:

Clustering - Alignment - Track reconstruction - DUT data analysis

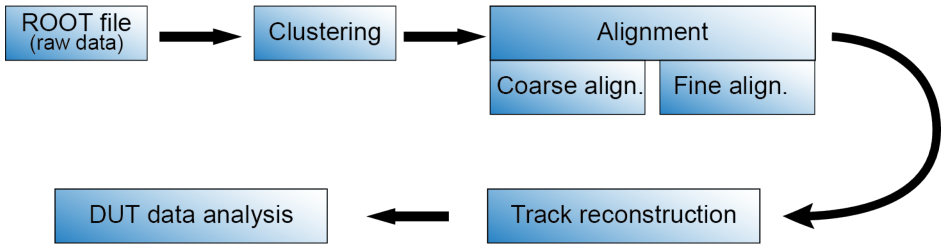

Figure 15: The Proteus analysis procedure

Clustering: when a single particle hits the detector plane, charge sharing effects and cross-talking lead to the activation of a pixel cluster, with which Proteus is working. The first step in the process consists in grouping the pixel hits into clusters. For further analysis, the geometric mean of the pixel positions inside the cluster is taken as the position of the hit.

Alignment: for track reconstruction purposes, the Proteus software uses configuration files given by the user to recreate the geometry of the setup. However, perfect knowledge of the detecting planes' positions isn't practically achievable. In order to improve the accuracy of the tracking, misalignments between the planes have to be accounted for. In Proteus, the alignment process is done in two steps: the coarse alignment and the fine alignment.

The coarse alignment procedure corrects interplanar offsets in the directions perpendicular to the beam (X and Y, see figure 15). It works by taking the cluster position distribution in every plane and fitting a gaussian curve on it. The first plane is then fixed as a reference for the rest of the setup. The offset between the reference plane and the next one is estimated by computing the difference between the two gaussian means. The resulting correction is applied to the second plane and the procedure is repeated between the third and second plane. The coarse alignment procedure is applied only between neighboring planes to reduce impact of scattering effects.

The next step is the fine alignment procedure, correcting finer offsets and rotations around the z-axis (beam axis). To this end, track residuals are obtained by computing the difference between the particle path hit position (the reconstructed path) and the position of the cluster associated to this track (the sensor's answer). The corresponding correction is then applied to the plane. The fine alignment is done separately for the X and Y directions.

Since misalignments corrected by this procedure have an effect on the track reconstruction, they have an effect on the correction itself. This is why the fine alignment process is a recursive method working with unbiased residuals: the plane being corrected is excluded from the track reconstruction and doesn't influence the residuals used for its correction.

Track reconstruction: the track reconstruction in Proteus is done with a recursive algorithm collecting cluster hits and extrapolating the particle path. Starting with the first plane, it takes a cluster and searches for clusters in the following plane inside a user-defined solid angle (cone). It then goes on to the next plane until the track is totally reconstructed. If several clusters are found within the angle, the track is bifurcated and the algorithm recursively computes all possible paths and keeps the one with the most associated clusters. If several candidates are available, a straight line fit is applied to each one of them and the one with the lowest χ^2 is kept. Once the track has been reconstructed, the corresponding clusters are not considered anymore.

To ensure accurate tracking, a hard cap is given by the user on the χ^2 so that only well-fitted, straight tracks are kept. All tracks going above this threshold are subsequently excluded.

Proteus also takes into account the possibility of a particle going through one or several planes without leaving a cluster by allowing the track reconstruction algorithm to bypass a plane without cluster in the angle and search in the following planes.

For more information about track fitting, refer to [36].

DUT data analysis: Proteus enables further processing of the informations obtained during track reconstruction. Depending on the requirements of the experiment, several analyzers are available to the user. For instance, a common task requiring Proteus is the efficiency analysis of a DUT inside a testbeam.

The efficiency analyzer works by comparing the "real" path of a particle (the reconstructed track) with the DUT answer to this particle. The algorithm starts by taking a reconstructed track under the χ^2 threshold defined by the user and extrapolating it to the DUT plane. The algorithm then searches for a cluster in the DUT to match to the track, using the following equation:

$$d = \sqrt{\left(\frac{x_{track} - x_{DUT}}{l_X/2}\right)^2 + \left(\frac{y_{track} - y_{DUT}}{l_Y/2}\right)^2} \tag{9}$$

$l_{X(Y)}$ is the size of the DUT sensor in the $X(Y)$ direction, $x(y)_{track}$ is the extrapolated position of the track on the DUT plane and $x(y)_{DUT}$ is the position of the associated cluster (computed as its geometrical mean). Taking $N_{matched}$ as the number of matched tracks and N_{total} as the total number of reconstructed tracks, the efficiency of the DUT is defined as follow:

$$\epsilon = \frac{N_{matched}}{N_{total}} \tag{10}$$

This efficiency algorithm can be used to observe the global DUT efficiency (pixel per pixel), as well as the efficiency at the sub-pixel level.

Another interesting property that can be estimated after matching of the tracks is the resolution of the telescope. If the DUT response is well known, the distance between the reconstructed track at the DUT level and the corresponding cluster in the DUT depends on the accuracy of the telescope. From this, it is possible to infer its maximal spatial resolution. For a perfectly accurate telescope in ideal conditions, the resulting curve would be a rectangular function with a width equivalent to the pixel width.

IV. Simulation and Analysis

1. Simulation

1.1 Setup layout

The FEI4 Telescope is recreated through AllPix. AllPix is a Geant4-based software used for the reconstruction of pixel detectors and simulation of a traversing particle beam [37]. It starts by modeling the telescope layout in 3 dimensions following the instructions of user-defined geometry files, defining the physical properties of every sensor plane as well as their positions relative to each other.

In the scope of this study, 2 types of sensor planes are defined: the FEI4 and the Mimosa26 detector. Their physical dimensions are based on their real-life counterparts. The layout of the telescope is based as well on the real-life telescope. The Mimosa26 planes are added 40 mm from the DUT, front and back. Finally, the DUT itself is an FEI4 detector. To get a more realistic layout, random offsets of up to 300 μm in the directions x, y and z have been applied to each plane. This helps represent small misalignments present in the experimental setup.

1.2 Digitizers

AllPix then assigns a digitizer to each plane. The digitizer simulates the electronic characteristics of a detector by converting the "analog" (in the scope of the simulation) hit in the sensor to a digital signal. At this step, various effects can be implemented, such as charge-sharing, crosstalk and trapping; the activation threshold is also defined in the digitizer. As a result, the response characteristics of a certain type of detector can be simulated in AllPix.

Three digitizers are used in the FEI4 simulation: the FEI4 and Mimosa26 sensor planes use each their own digitizer. As for the DUT FEI4 plane, it uses a monte-carlo digitizer: no electronics are simulated, and any energy released in the pixel is considered as a hit, with perfect accuracy. This means that the hits recorded in the DUT show accurately the path of the traversing particle.

1.3 Beam profile

Finally, AllPix simulates particles going through the telescope with a user-defined beam profile. Effects such as scattering and secondary particles creation are also simulated during this step.

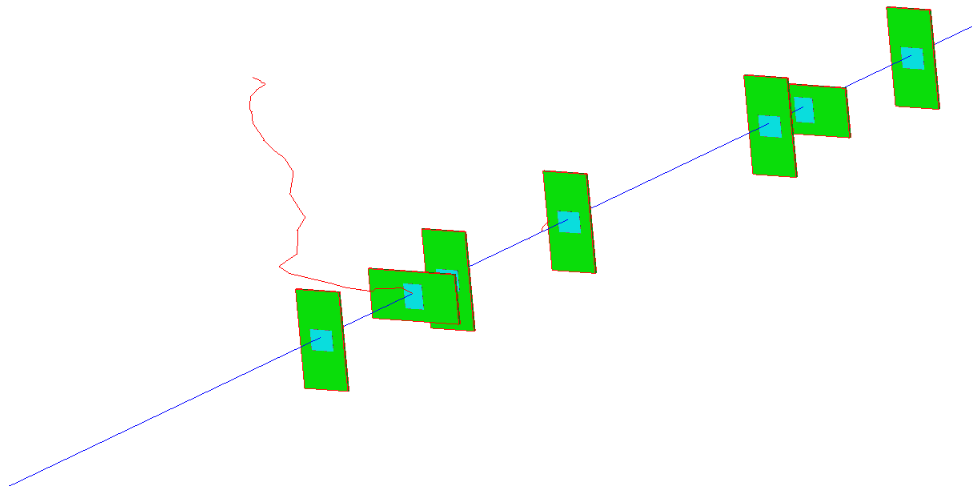

Figure 16: 3D visualization of the FEI4 telescope as recreated by AllPix. The plane sensors are shown in green, with 3 on each side of the DUT in the middle. The FEI4 chip itself is shown in blue. Per Geant4 standard, the blue path represents a positively charged particle. A secondary, negatively charged particle is scattered.

For the FEI4 simulation, the beam is flat, with a 16'800 x 10'656 μm^2 rectangular section and no angular distribution. These dimensions have been selected to correspond to the overlap of the detection planes, so that no geometric effect applies during the simulation: all planes have the same amount of tracks going through. The particles used are 180 GeV π^+.

To simulate ionization, AllPix computes the trajectory of a particle. At regular intervals along the path, the eventual energy deposit is computed. The steps are reset at the interface of materials (for instance, between air and silicon).

For each setup (with and without Mimosa26), 500'000 events are simulated. The Mimosa digitizer active depth is 5 μm, meaning that energy deposit are detected only in this zone. Since the step counting is reset at material interface, a step length of 4.9 μm has been selected to ensure that no energy deposit is missed by the Mimosa26 planes. The resulting files are then converted into a Proteus-readable format for the analysis.

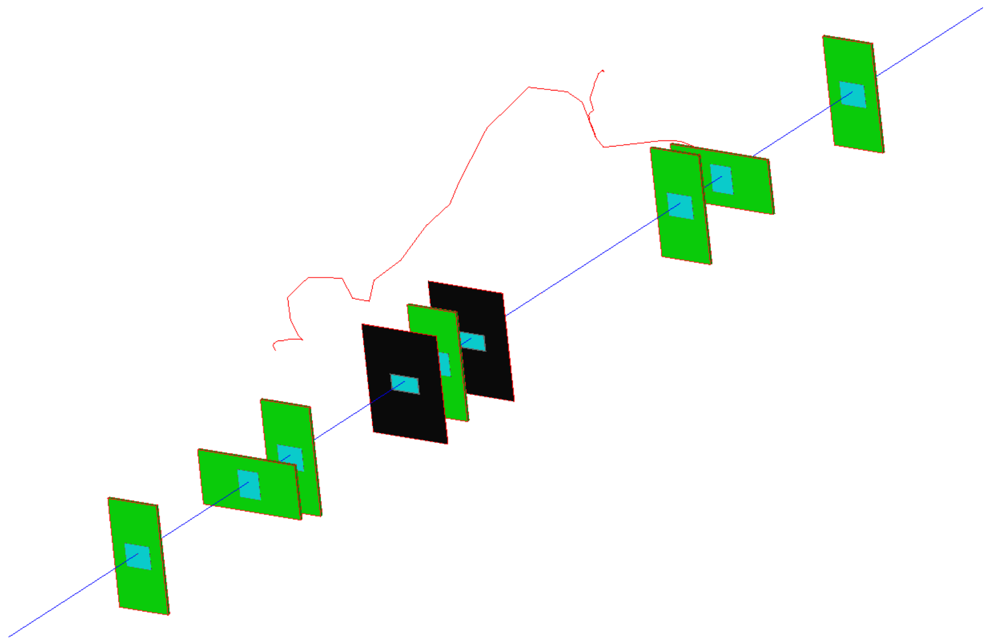

Figure 17: 3D visualization of the Mimosa telescope as recreated by AllPix. The added Mimosa26 planes, displayed in black, are placed on each side 40 mm from the DUT.

2. Proteus Analysis

The raw data produced by AllPix is analyzed in Proteus. Since the offsets are known, the corrections are directly applied, without the need to go through the alignment procedure. The analysis has been done separately for the two setups (with and without Mimosa26), and no masks were applied. For clarity purpose, the telescope layout with only FEI4 detectors is called "FEI4 telescope", while the telescope layout with added Mimosa26 is named "Mimosa telescope".

2.1 Reconstruction

The correct alignment and reconstruction of the relative positions of the planes are verified with correlation plots, where the cluster positions (in X or Y) are compared between two planes. If the telescope is well aligned, a cluster position in a plane should approximately correspond to the cluster position in the following plane (for the same track). The correlation plots show the difference in pixel pitch between the X and Y directions in the FEI4

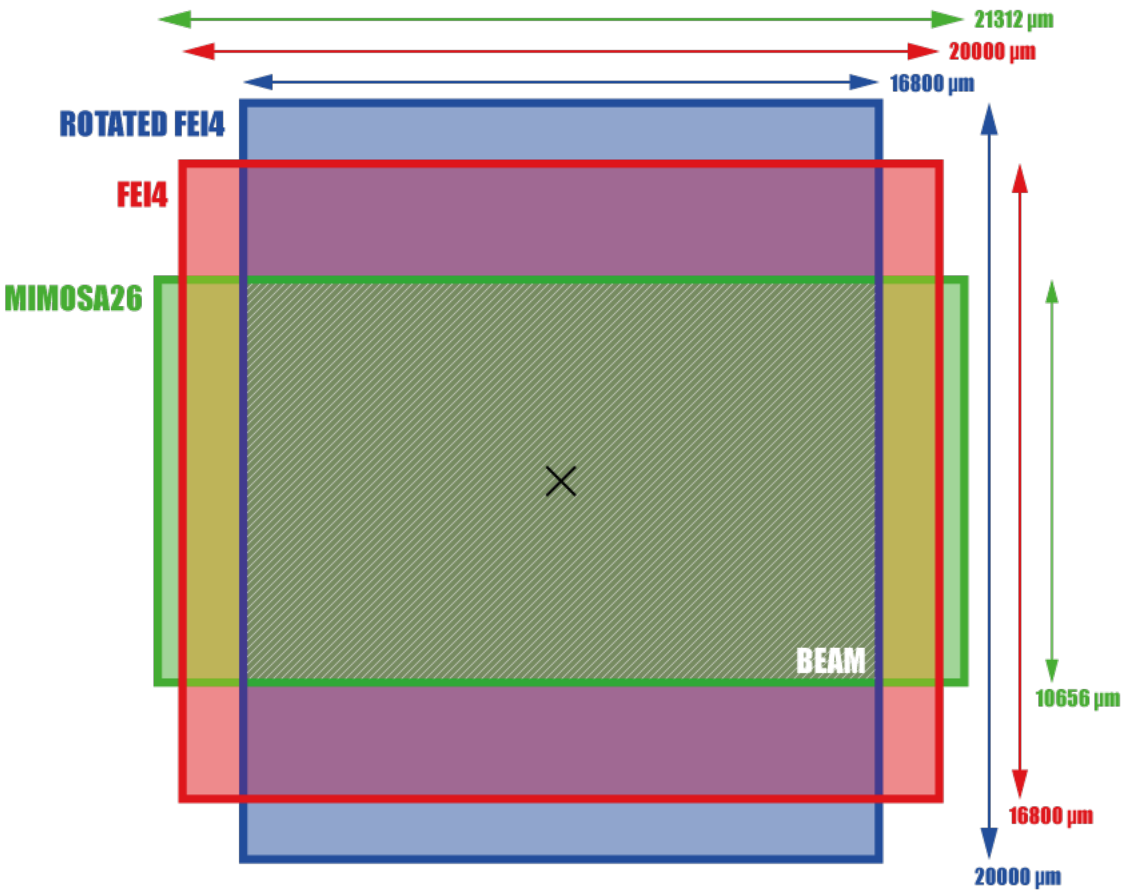

Figure 18: Cross section of the overlapping detectors: the FEI4 planes, rotated FEI4 planes and Mimosa26 planes. The beam has been designed to cover their overlap. For a given number of events, the same number of tracks is going through each detector. This cross section is to be compared to the detector occupancy, described further below.

sensor, as well as the higher spatial accuracy of the Mimosa26 sensor.

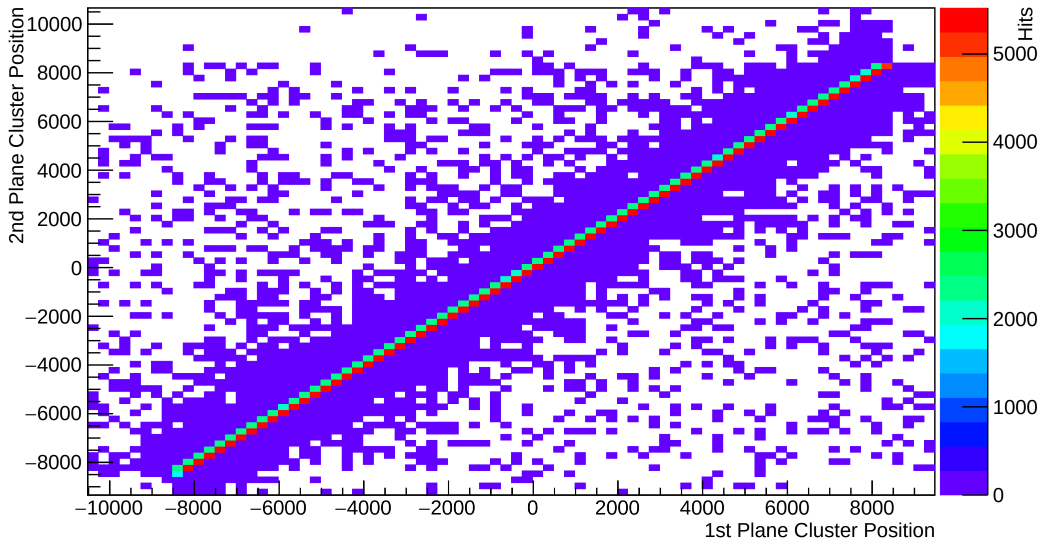

Figure 19: Correlation plot along the direction X, between two FEI4 planes.

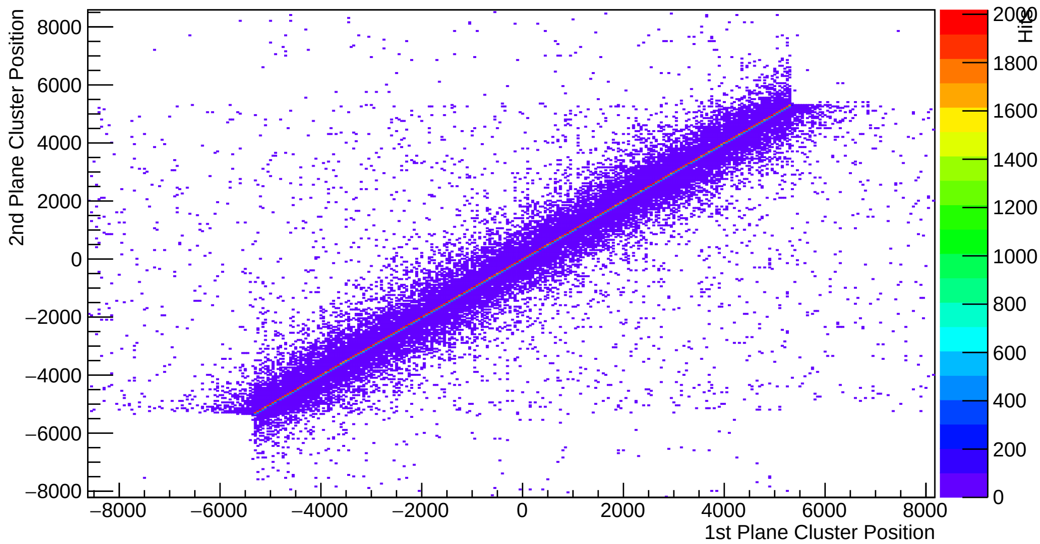

Figure 20: Correlation plot along the direction Y, between two FEI4 planes. Difference in spatial resolution between the X and Y directions can be observed because of the finer points in Y.

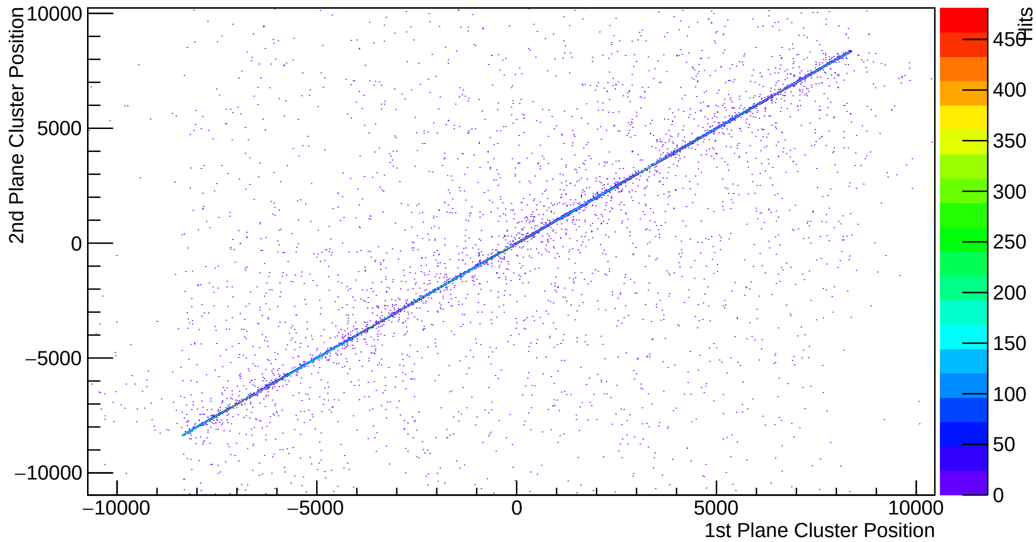

Figure 21: Correlation plot along the direction X, between two Mimosa26 planes.

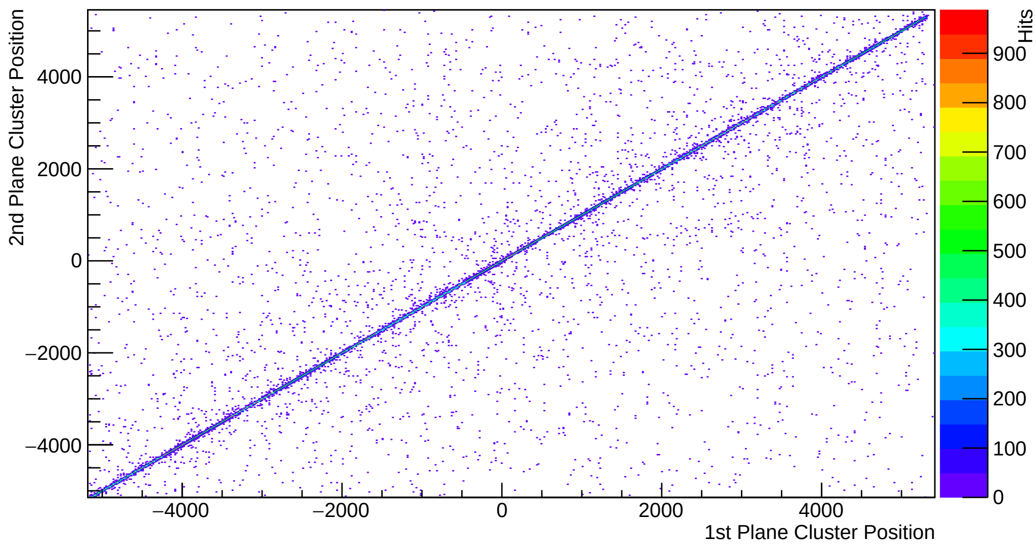

Figure 22: Correlation plot along the direction Y, between two Mimosa26 planes. Compared to the FEI4, Mimosa26 correlation points are much finer, denoting higher spatial resolution. In this case, X and Y directions are similar.

To verify that the correct beam profile has been used, occupancy plots are created for every plane, showing the hit positions inside the sensor. The beam size and shape can be observed in these plots. Differences in pixel size between the FEI4 and Mimosa26 planes can also be inferred by looking at the occupancy of each type of detector, where the higher spatial accuracy of the Mimosa plane is quite clear.

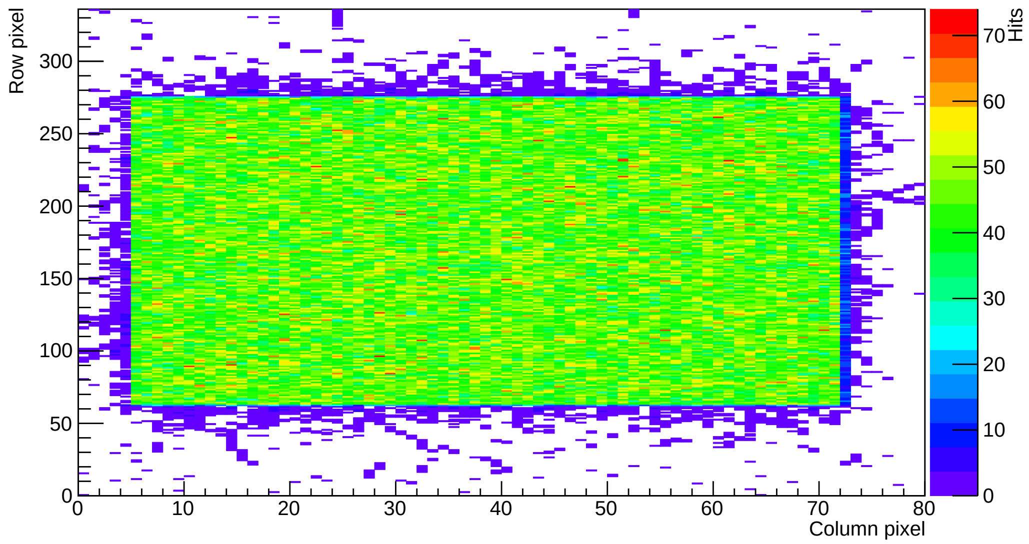

Figure 23: Occupancy of an FEI4 plane. The non-rotated plane isn't fully covered by the beam.

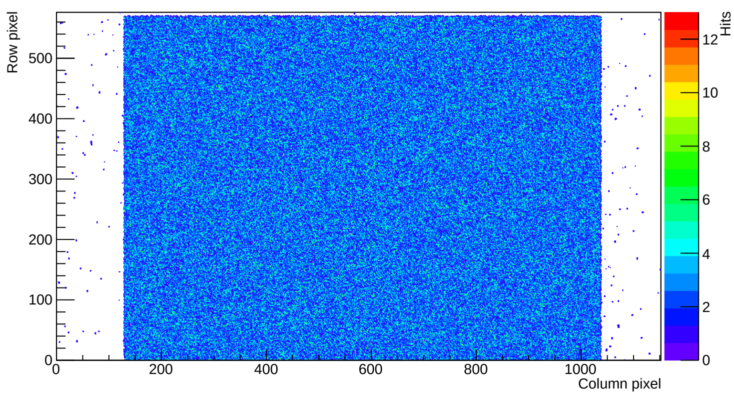

Figure 24: Occupancy of a Mimosa26 plane. Note that the sensor plane is fully covered in the Y direction by the beam.

For each cluster, the number of pixel activated in a sensor plane is called cluster size. Ideally, each cluster would have a size of 1 pixel. However, effects such as noise, charge-sharing, scattering and secondary particle production can lead to several pixel registering a hit. The cluster size distribution of a given detector can provide some insight into its operation.

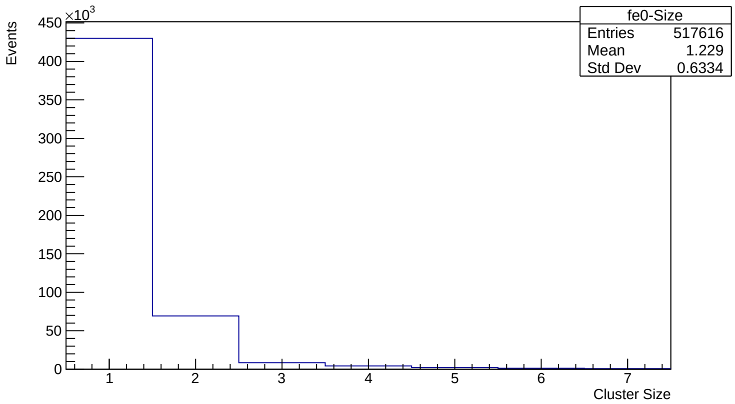

Figure 25: Cluster size distribution of an FEI4 plane.

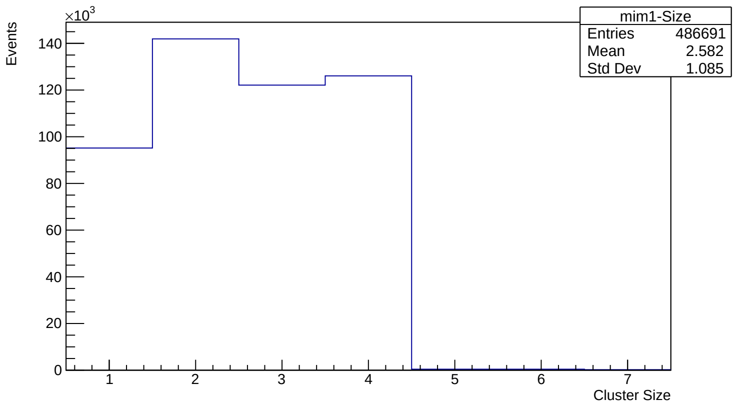

Figure 26: Cluster size distribution of a Mimosa26 plane.

We see from the cluster size distribution that the FEI4 planes have typically 1 pixel in a cluster (mean: 1.23 pixels). This can be explained by the rectangular pixel pitch, where a single hit can more easily activate the pixels above and/or below the central pixel (separated by 50 μm) than its lateral-neighboring pixel (separated by 250 μm). So the most common case for a cluster size higher than 2 in an FEI4 is the activation of those neighboring above/below pixels.

This can be put in contrast with the Mimosa26 cluster size. As expected, the smaller pixel pitch and square shape lead to a higher average cluster size; moreover, no direction is preferred in this case, as the 4 neighboring pixels are all at the same distance from the middle pixel's center. A particle passing through the far corner of a Mimosa26 pixel can more easily activate its 3 neighbors.

2.2 Tracking

During the tracking phase, no cuts are applied to the χ^2 of the reconstruction. For the track to be valid, it is required that all reference planes are involved in the reconstruction (6-planes-track in the FEI4 telescope, 8-planes-track in the Mimosa telescope).

To further check correct positioning of the planes and to ensure reasonable track reconstruction, residual plots are produced.

In a perfectly aligned simulation without scattering, the residuals are expected to be shaped as a dirac δ function centered on the origin. Misalignments, scattering, noise and other experimental effects broaden the peak to form a gaussian curve with a mean of 0. The FEI4 pixel shape means that a broader distribution is expected on X than on Y. Moreover, the rotated FEI4 planes in the telescope create a 5-peak structure on X, with the middle peak centered on the origin; when added, the Mimosa26 planes should compensate for this effect with their higher spatial resolution.

As seen on figure 29, the small offsets used at AllPix shift the 5-peak structure, leading in fact to a 6-peak structure slightly off-center. This effect has also been observed in real data.

As expected, the figure 30 shows a narrower distribution on Y for the FEI4 planes and the compensation of the 5-peak structure by the Mimosa26 planes.

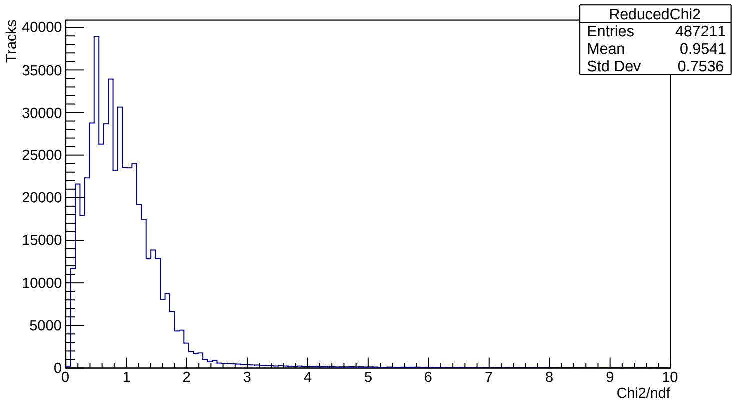

Figure 27: χ^2 over number of degrees of freedom distribution of the track reconstruction with the FEI4 telescope. The ideal χ^2/ndf should be close to one, which is the case here. Effects due to the FEI4 pixel shape are hinted in this histogram (peak formation).

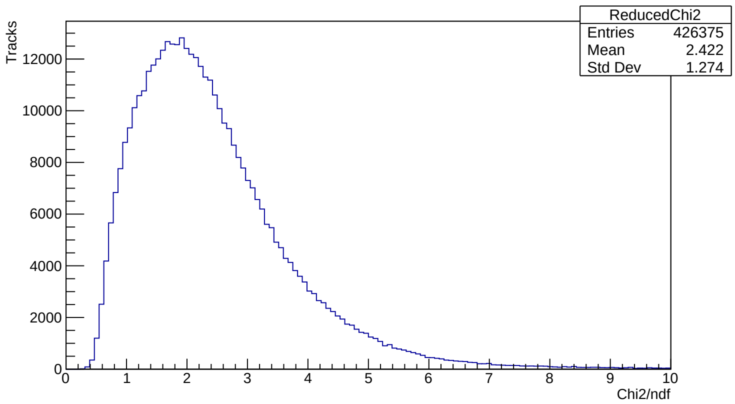

Figure 28: χ^2 over number of degrees of freedom distribution of the track reconstruction with the Mimosa telescope. The smaller pixel size means a larger error compared to the FEI4 telescope, pushing the χ^2/ndf to larger values.

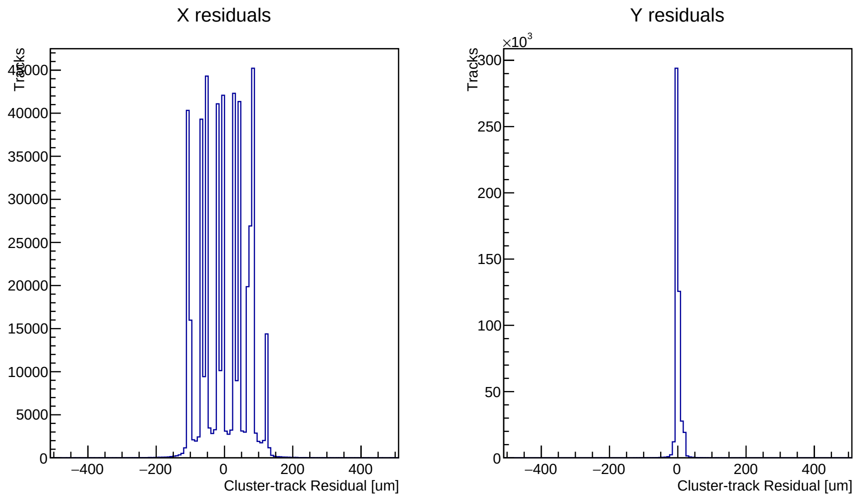

Figure 29: Residuals of an FEI4 plane in the FEI4 telescope.

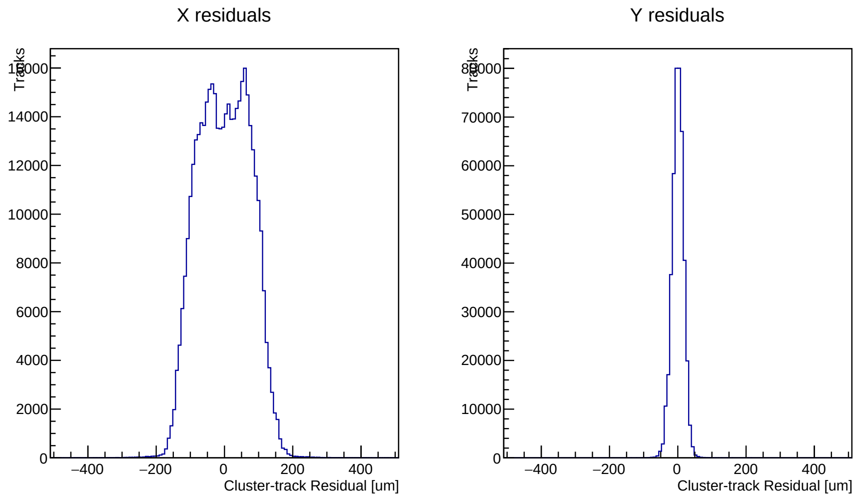

Figure 30: Residuals of an FEI4 plane in the Mimosa telescope.

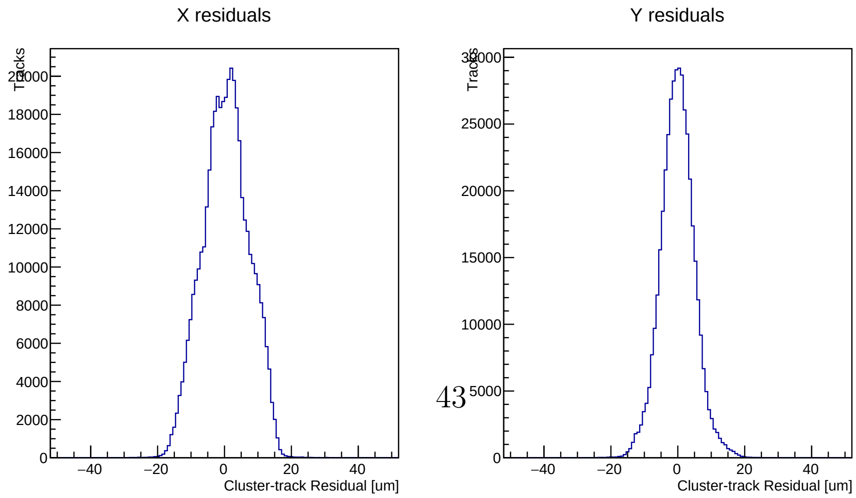

Figure 31: Residuals of a Mimosa26 plane in the Mimosa telescope.

2.3 Resolution estimation

After clustering and tracking, the track produced are matched to the DUT hits. Since the simulated DUT is perfectly accurate, the distance between the track and its matched DUT cluster is a good estimation of the telescope's precision. It should be noted that since the DUT uses a monte-carlo digitizer, its cluster size is always 1 (the pixel though which the particle is going). Moreover, only single-track events are considered. Finally, the track is excluded if the square of its distance to the DUT cluster, weigthed by its distance to the center of the pixel, is bigger than 0.4 μm^2. These cuts ensure that no secondary particles are taken into account during the resolution estimation.

Of importance in these histogram is the peak-structure along the X direction in the FEI4 telescope. It is a known effect observed in previous simulations and real data analysis that comes from the FEI4 pixel shape. To mitigate the detector's lower accuracy in the X direction, 2 planes are rotated at 90°. While the resolution in this direction is improved, this leads to a five-peak structure , where the peaks are separated by 50 μm (the pixel length along X in the rotated planes). In real data, this effect is reduced by misalignments, small rotations and other factors, leading to the dampening of the peaks and their shift (forming in fact a 6-peak structure). This can also be observed in our simulation, as small offsets have been added.

A result of adding Mimosa26 planes to the telescope is that the structure disappears, as the Mimosa compensate for this effect by setting the track at a sub-FEi4-pixel accuracy, effectively canceling the pixel pitch effect.

To estimate the resolution, the cluster-track distance histograms are fitted with a mirrored S-curve, using the following equation:

$$A(\mathrm{erf}(\frac{x+\mu}{\sigma}) - \mathrm{erf}(\frac{x-\mu}{\sigma})) \tag{11}$$

$$\mathrm{erf}(x) = \frac{1}{\sqrt{\pi}} \int_{-x}^{x} e^{-t^2} dt \tag{12}$$

with A the amplitude of the fit, μ the position of the peak and σ the resolution of the telescope. erf(x) is the error function, defined in (12).

The fitted cluster-track distance plots are shown in figures 32 through 35. The results are summarized in the table 1.

The 5-peak structure in the FEI4 telescope X dimension complicates the fitting of the histogram; however, although the selected fit doesn't closely follow the data in this case, it is still usable at the edge of the distribution, where the resolution is estimated. To be noted that in this study, the X cluster-track distance plot shows a 4-peak structure. As stated above, the misalignments introduced at the AllPix level and corrected by Proteus create in fact a 6-peak structure; after the cuts, two peaks are erased, leading to the skewed 4-peak structure seen in figure 32.

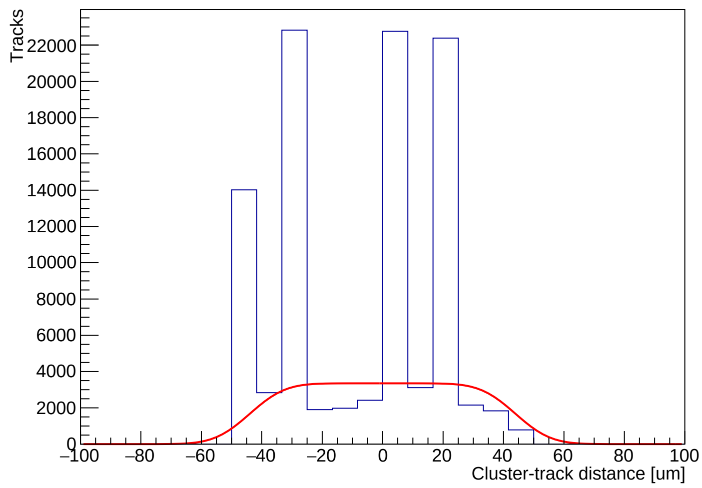

Figure 32: FEI4 telescope: cluster-track distance histogram along X at the DUT with fitting curve.

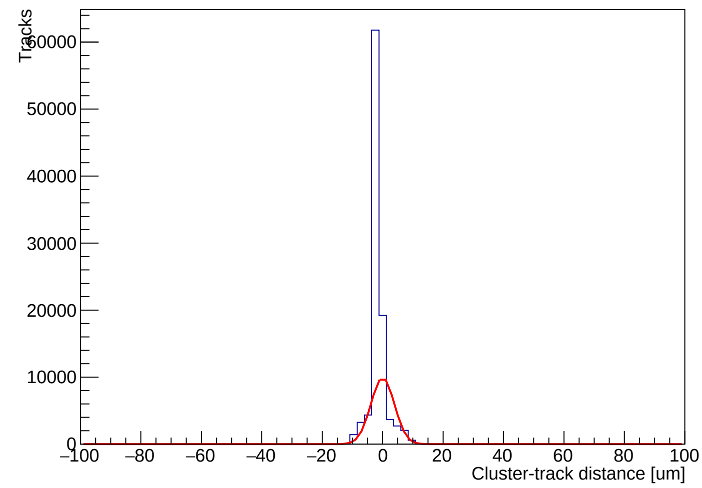

Figure 33: FEI4 telescope: cluster-track distance histogram along Y at the DUT with fitting curve.

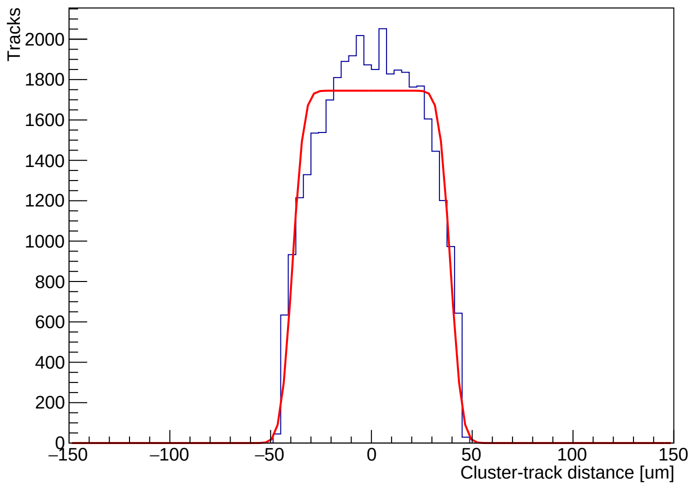

Figure 34: Mimosa telescope: cluster-track distance histogram along X at the DUT with fitting curve.

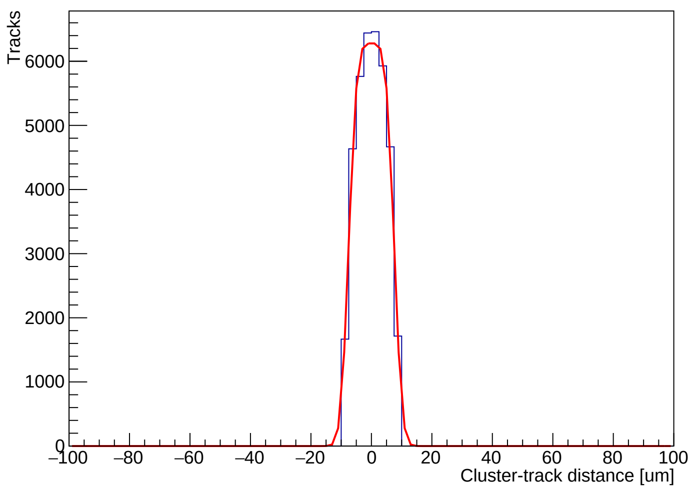

Figure 35: Mimosa telescope: cluster-track distance histogram along Y at the DUT with fitting curve.

Telescope	Entries	Resolution [μm]	Error [μm]	Improvement
FEI4 X	98998	13.0	0.4	106.3%
Mimosa X	37277	6.3	0.2	
FEI4 Y	98998	5.44	0.04	86.9%
Mimosa Y	37277	2.91	0.08	

Table 1: Fit results

As expected from the FEI4 pixel shape, the FEI4 telescope is more accurate along the Y direction, with a resolution of 5.44 μm compared to 13 μm in X (41.8%). The Mimosa telescope also follows this trend (46.2%), mitigated by a greater improvement on the X resolution than on the Y. This can be explained by the higher pixel pitch difference in X: 18.4 μm to 250 μm (7.4% of the FEI4 length).

Another notable difference between the two setups is the absence of the 5-peak structure in the mimosa telescope, as seen on figure 34. The finer granularity of the Mimosa26 planes gives a more accurate tracking and compensates for the aformentioned effect.

These results are obtained with several realistic parameters, although improvements can be added. For instance, small rotations can be implemented in AllPix to simulate practical conditions, in addition to the offsets. This would have the added advantage of damping furthermore the 5-peak structure, facilitating the resolution estimation along the X direction. The digitizers can also be fine-tuned to add effects not yet taken into account (notably noise on the Mimosa26 planes). Moreover, practical conditions have to be taken into account when implementing new hardware. The distance of 40 mm between the Mimosa26 planes and the DUT could be difficult to achieve because of the DUT baseplate/box size. The resonance of the telescope structure could also be a factor in the accuracy of the setup. A modal analysis has been conducted to study this point.

V. Modal Analysis

1. Theory

1.1 Introduction

Mechanical systems are subject to mechanical resonance effects, resulting in structural deformations. Resonant frequencies of bridges are studied to ensure that oscillations induced by the environment do not lead to structural damage, or even full collapsing. In the scope of high precision physics experiments, these studies can be necessary to observe, and eventually prevent, the effects of resonance on the accuracy. Such a modal analysis has been performed on the FEI4 telescope in its usual environment, the CERN SPS H8 beamline.

1.2 Mechanical systems

Resonance properties of a structure can be described using the "modal" model [38, 39, 40]. In this model, modes are inherent properties of the mechanical system determined by material properties, such as mass, damping, stiffness and the structure's boundary conditions. The modes themselves are described by a modal frequency and damping.

A single-degree-of-freedom (SDOF) oscillating system is described by the following equation:

$$f(t) = m\ddot{x}(t) + c\dot{x}(t) + kx(t) \tag{13}$$

where $x(t)$ is the position of the mass m with respect to its equilibrium position ($f(t) = 0$), c the damping coefficient, k the stiffness and $f(t)$ an externally applied force. Correspondingly, the $m\ddot{x}(t)$ group is the inertial force, $c\dot{x}(t)$ the damping force and $kx(t)$ the restoring force.

When applying a Laplace transformation, the equation (13) becomes:

$$Z(s)X(s) = F(s) \tag{14}$$

In the equation (14), $Z(s)$ is the dynamic stiffness:

$$Z(s) = ms^2 + cs + k \tag{15}$$

The displacement $X(s)$ (output) and the force $F(s)$ (input) are linked by the transfer function $H(s)$: $X(s) = H(s)F(s)$, which is then equivalent to the inverse dynamic stiffness:

$$H(s) = \frac{1}{ms^2 + cs + k} \tag{16}$$

The poles of the system are given by the roots $d(s) = ms^2 + cs + k$ of the transfer function's denominator. Moreover, in mechanical systems, the damping coefficient c is usually very small, so that the equation poles are a complex conjugate pair:

$$\lambda = -\sigma \pm i\omega_d \tag{17}$$

where σ is the damping rate. $\chi\omega$ represents the damped natural frequency; the damping factor χ is defined as:

$$\chi = \frac{c}{\sqrt{2km}} \tag{18}$$

Although there are several damping possibilities, the underdamped case ($\chi < 1$) is the only one relevant to mechanical modal analysis.

If we replace the Laplace variable s by $i\omega$ in (16), we get the Frequency Response Function (FRF):

$$H(\omega) = \frac{1}{(k - m\omega^2) + ic\omega} \tag{19}$$

Without the damping parameter $ic\omega$, the FRF would go to infinity when the system is at natural frequency $\omega \to \omega_n = \sqrt{k/m}$.

As can be seen from their definitions, the transfer function is the Laplace transform of the output divided by the Laplace transform of the input, whereas the FRF is the Fourier transform of the output divided by the Fourier transform of the input. This relation can help to understand mathematically the modal analysis.

During a modal test, an input (mechanical excitation) is applied on the system and the output is measured. The FRF can then be computed and fitted to obtain the poles in the Laplace domain (transfer function).

Finally, more realistic multiple-degree-of-freedom (MDOF) systems can be represented as linear superpositions of SDOF systems, meaning that the previous steps stay valid. In this case, the dynamic stiffness becomes a matrix:

$$\boldsymbol{H}(s) = [\boldsymbol{M}s^2 + \boldsymbol{C}s + \boldsymbol{K}]^{-1} \tag{20}$$

The resulting parameters are equivalent, with the addition of a displacement vector defining the mode shape of the system.

2. Modal Testing

2.1 Background measurements

The modal analysis is done in two parts: background measurements and modal measurements. These were done using a Müller-BBM MKII spectrum analyzer, different seismic accelerometers for vertical displacements, 3-axial accelerometers for response measurements and an impact hammer 086D20 for input. For the analysis, different points of interest are defined on the FEI4 telescope, as shown on figure 36. The "right" and "left" points are respectively the downbeam and upbeam mechanical arms holding the reference planes. The "table" point is the baseplate and the "base" point is the support plate holding the telescope.

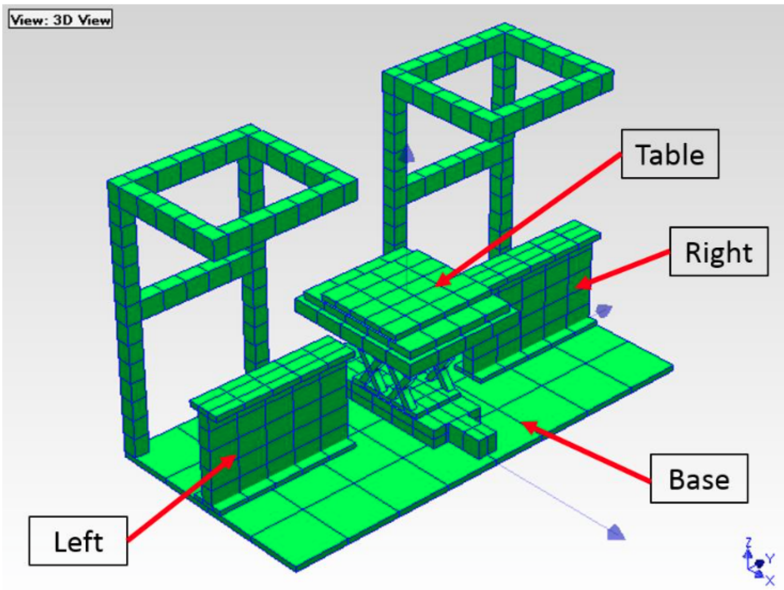

Figure 36: 3D model of the FEI4 telescope with the accelerometer locations.

For background measurements, seismic accelerometers have been placed on the points of interest and left measuring during 30 minutes. The resulting power spectral density (PSD) is then inferred. Its RMS is integrated to obtain the vertical displacement spectrum, as shown on figure 37.

2.2 Modal test

To observe the transfer functions of the telescope, the 3-axial accelerometers are installed on the different points of interest. An input is provided with the impact hammer on the base. Each point has been measured three times,

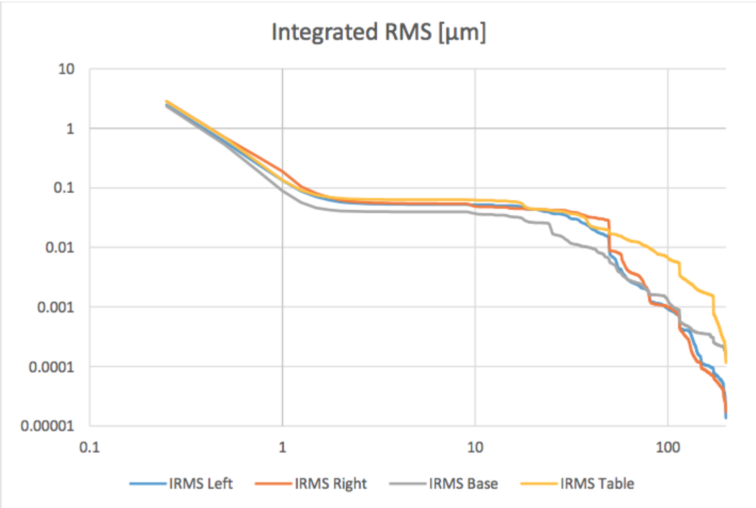

Figure 37: Integrated RMS of the PSD on 4 points of interest.

and the magnitudes of the transfer function are shown in figures 38 through 40.

Finally, the data are combined to determine the different vibration modes and their relative damping. The results for the FEI4 telescope are summarized on the table 41.

3. Conclusion

From the table 41, we can see that the FEI4 telescope is sensitive to vibrations on several modes, notably around 45.9, 57.7, 71.4 and 73.6 Hz.

As shown by the low relative damping, the whole installation's resonance frequency is around 71.4 Hz, while some component can resonate at other frequencies: the 45.9 Hz mode corresponds to the oscillation of the superstructure over the arms, especially the right part. The 57.7 Hz mode is the at the resonance frequency of the "base" point. Finally, the 73.6 Hz mode corresponds to an oscillation of the left part of the support base.

Those frequencies are already in the low part of the background IRMS, meaning that the FEI4 telescope is already stable enough for the current operations. However, in anticipation of its resolution upgrade as well as to ensure optimal performance, it has been upgraded with a new honeycomb-structure support table and rubber bumpers to provide a higher passive damping and ease of operation.

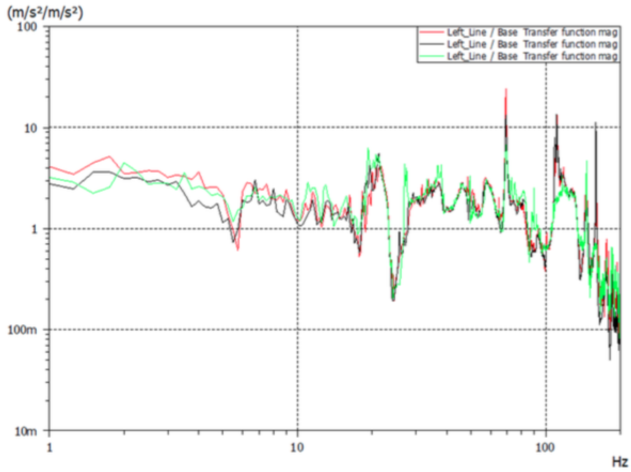

Figure 38: Base to left arm transfer function.

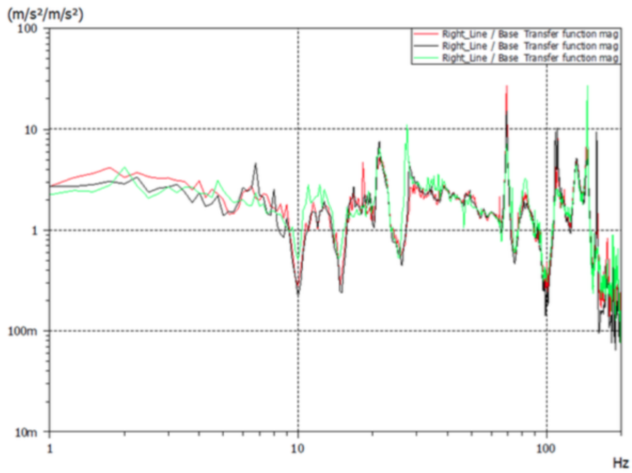

Figure 39: Base to right arm transfer function.

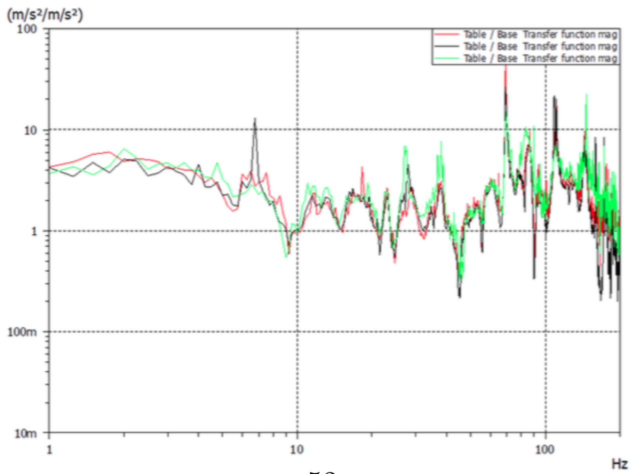

Figure 40: Base to table transfer function.

Frequency Hz	Damping Hz	Damping (%)
5.5	0.091	1.69
9.2	0.112	1.22
9.8	0.113	1.15
11.9	0.183	1.54
14.6	0.242	1.66
17.5	0.417	2.38
21.1	0.432	2.05
23.3	0.532	2.28
28.1	0.903	3.21
29.5	0.71	2.4
38.6	0.9	2.33
40.9	0.554	1.36
43.3	0.84	1.94
45.9	0.375	0.818
51.5	0.816	1.59
57.7	0.399	0.69
67.2	1.54	2.29
71.4	0.139	0.194
73.6	0.419	0.57
75.5	1.14	1.51
78.8	1.35	1.72
85.4	2.03	2.38
90.2	1.33	1.48
101	2.32	2.28

Figure 41: Damping of the FEI4 telescope for the different vibration modes.

VI. Conclusion

Mimosa26 planes produced by the IPHC Strasbourg have been discussed to be used in complement with the FEI4 planes so as to improve the spatial resolution of the Geneva FEI4 telescope.

In this study, setups with and without Mimosa26 detectors have been simulated with the Geant4-based AllPix simulation software, the results analyzed with the Proteus analysis software and then compared to offer qualitative and quantitative insight into the potential improvements.

Quantitative analysis suggests an improvement in resolution of 106.3% in the X axis, bringing it from 13.0 μm to 6.3 μm, and 86.9% in the Y axis, bringing it from 5.44 μm to 2.91 μm. Moreover, qualitative analysis suggests that residual patterns observed in previous simulations are further reduced by the use of the new sensors. Compared to test-beam data, the FEI4 telescope resolution corresponds to expected values. Moreover improvements of this order were expected for the Mimosa telescope. However, as it stands now, the goal of sub-micron accuracy isn't yet achieved. To this end, additional upgrades could be planned to improve furthermore the FEI4 telescope.

This study could be further refined by various means. Some starting points would be to: add statistics to improve the resolution fitting, change configurations of the telescope to optimize placement of the planes, find the optimal distance between the DUT and the Mimosa26, modify the digitizers to simulate a more realistic behavior, and add small rotations in addition to the offsets. Ultimately, results of this study should be compared with test-beam data once the implementation of the Mimosa26 has been done, as to gain some insight for future simulations and resolution studies.

Modal analysis has been conducted on the FEI4 telescope to study the effects of resonance and background vibration on its accuracy. Several resonance frequencies have been found, although none correspond to typical background input, limiting the influence of seismic and human activity on the precision of the telescope's operation. However, in the scope of the telescope's spatial resolution upgrade, new vibration-damping material has been installed to ensure smooth operation even into sub-micron resolution levels.

Appendix

1. DUT Box Study

1.1 Design

A new DUT box has been built for the FEI4 telescope in order to upgrade it. Several requirements have been considered to improve upon the previous iteration:

- More height to accommodate the new DAQ system (Caribou)
- Use of testbeam-compliant components, with as little metal as possible
- Fixed parts for the cooling tubes and cables, for ease of manipulation
- Improved insulation around the tubes/cables openings

The box dimensions have been adapted to follow these requirements. Insulating foam has been used for the structure, ensuring robustness with a light weight and no interference with the testbeam. For the interface between tubes/cables and the box, two patch panels have been devised. They are attached by aluminum clamps to the main body, which allows manipulations inside the box without moving the cables and tubes. The cable patch panel is a "guillotine" system closing on the cables with insulating foam and can accommodate various sizes and numbers of cables. A structure has also been installed on the baseplate to allow bundling of the cables for ease of manipulation.

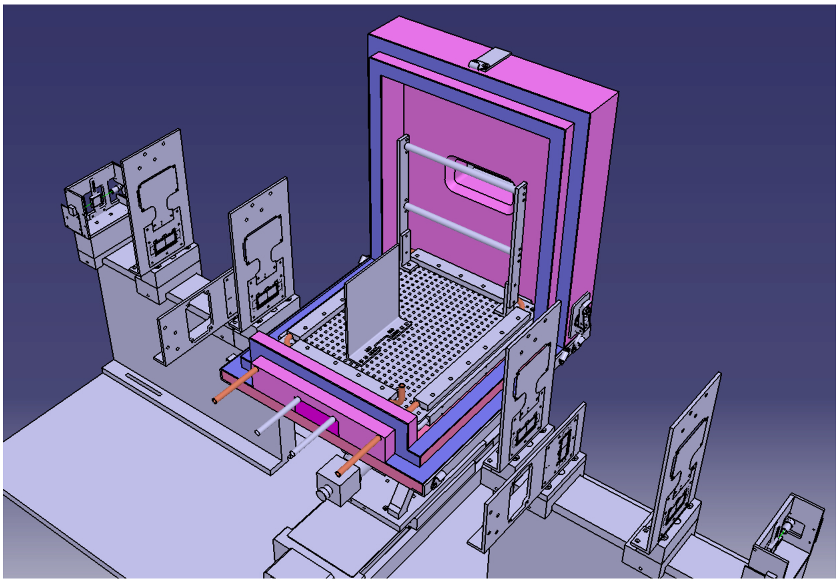

Figure 42: Computer design for the FEI4 DUT box (open). The silicon-oil cooling tube is in grey, the nitrogen gas tube is in orange.

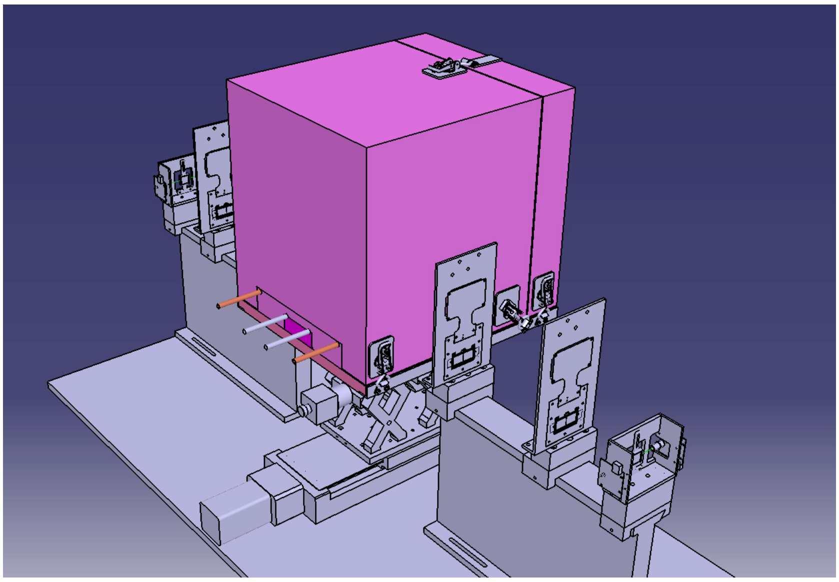

Figure 43: Computer design for the FEI4 DUT box (closed).

The box is cooled through the baseplate by a silicon-oil chiller. Humidity levels are managed by injection of nitrogen gas. The air conduct goes around the baseplate to cool down the gas before flowing it into the box.

1.2 Thermal study

The testing has been conducted at CERN in the SR1 laboratory. An CCPD plane has been installed on the baseplate and linked to it with copper tape to provide a better thermal conduction, as can be seen on figure 44.

Four temperature sensors have been installed on several points of the setup. The air temperature inside the box is measured by the "Box Air" sensor and the baseplate temperature by the "Baseplate" sensor. Additionally, the air dryness is monitored by a humidity sensor to ensure that no condensation occurs. The two remaining thermometers have been placed on the FEI4 chip and the HVCMOS sensor, as seen on figure 45.

For the test, the detector is switched on and then dry air is pumped in the box. Once the desired humidity level is reached (1.4%), the airflow is reduced to avoid damaging the sensitive wire bonds. Finally, the chiller is fully engaged to reach minimal temperature. Figure 46 shows the evolution of the temperature with the time. The first part of the test is described with more details in the figure 47.

The full cooling of the box takes approximatively 90 minutes (1h30). The temperatures reached at this point are summarized in the figure 48.

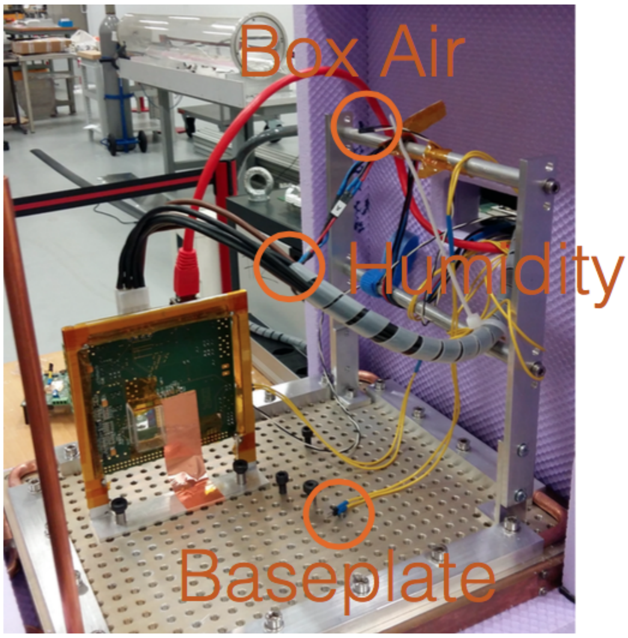

Figure 44: Temperature and humidity sensors in the DUT box. Note the copper tape linking the detector to the baseplate.

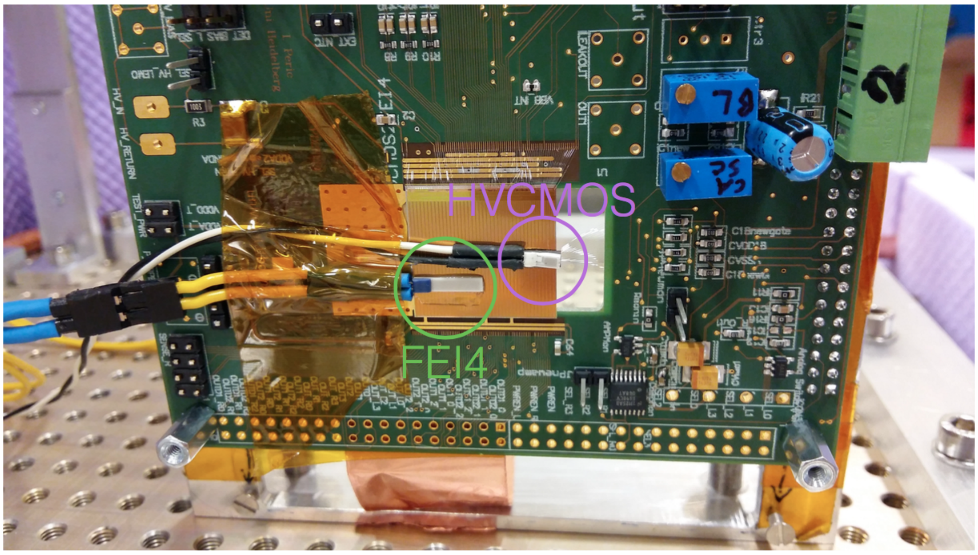

Figure 45: Temperature sensors on the FEI4 and HVCMOS. The wire bonds can be clearly seen on this picture.

The setup has also been observed with an infrared camera to detect points of thermal loss. As expected, the most vulnerable parts are the patch panels, where cables and tubes connect to the box (figures 49 and 50), and the

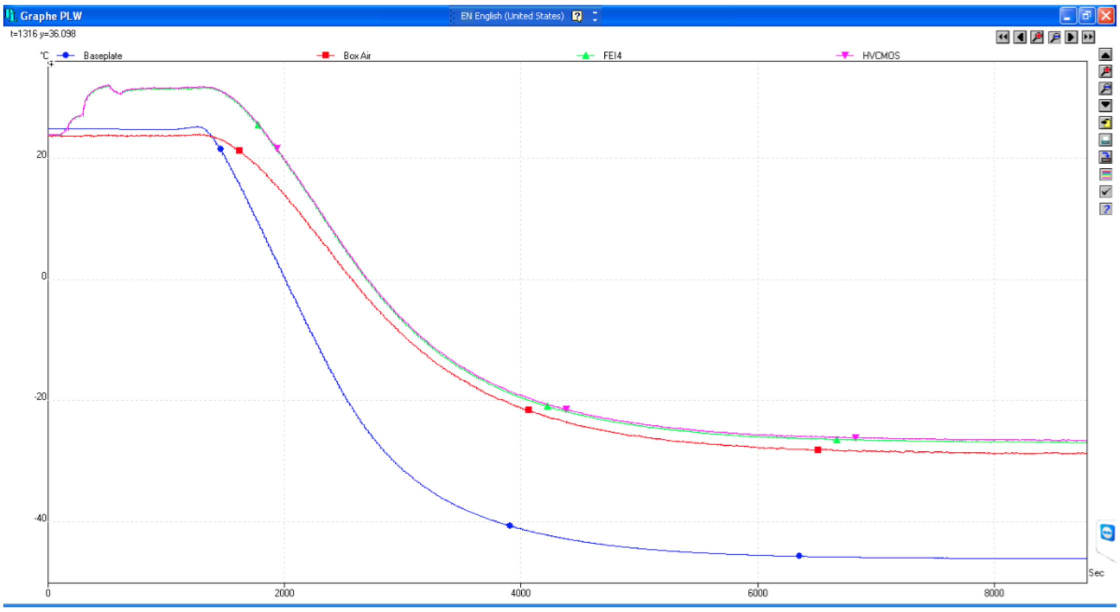

Figure 46: Temperature measures in the DUT box.

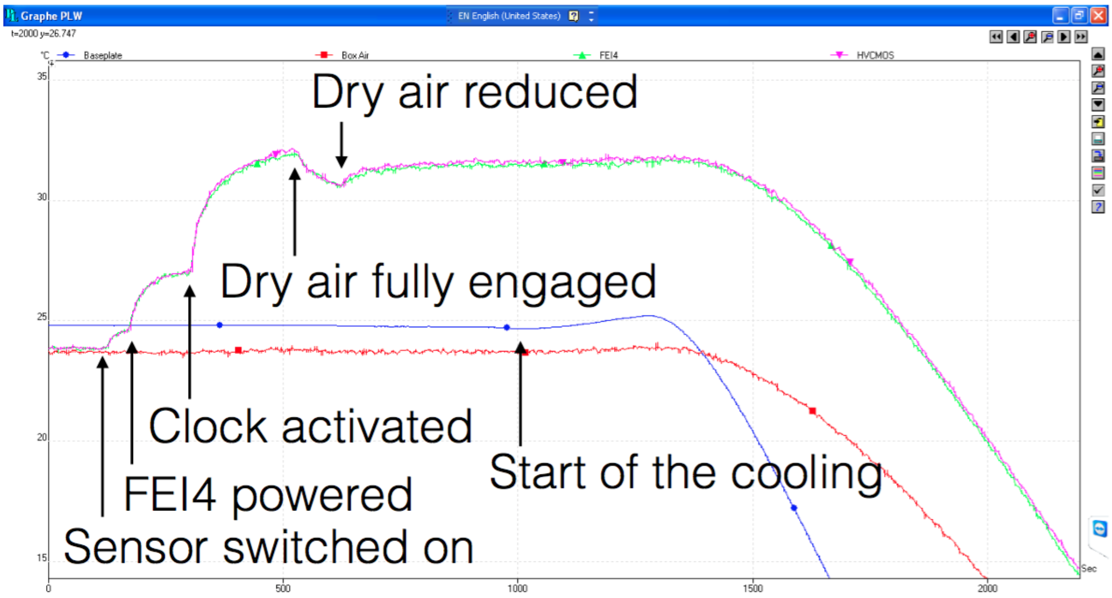

Figure 47: Detail of the temperature with the different steps annotated.

junction between parts of the box (figure 51). Some minor losses were also observed around the dry air output.

Sensor	Temperature
Baseplate [°C]	-46.10
Box air [°C]	-28.71
FEI4 [°C]	-26.93
HVCMOS [°C]	-26.60

Figure 48: Temperatures reached after full cooling.

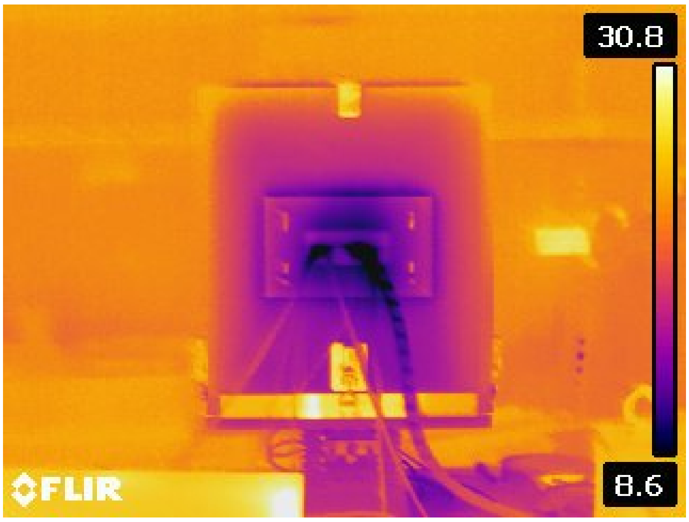

Figure 49: Infrared picture of the cable patch panel.

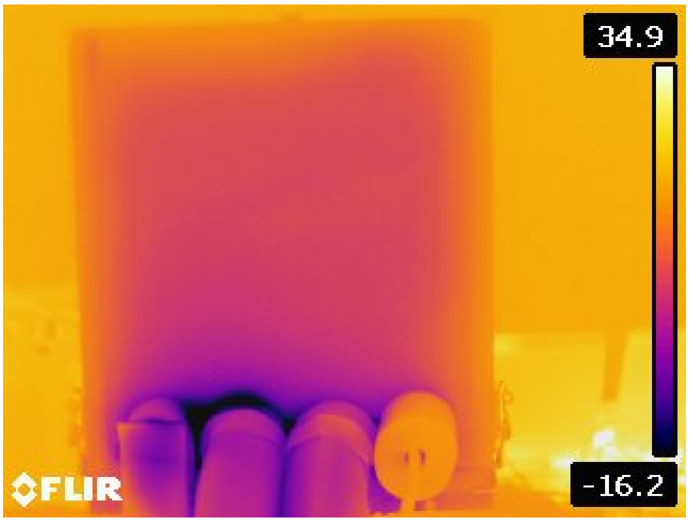

Figure 50: Infrared picture of the cooling patch panel. Note the temperature scale.

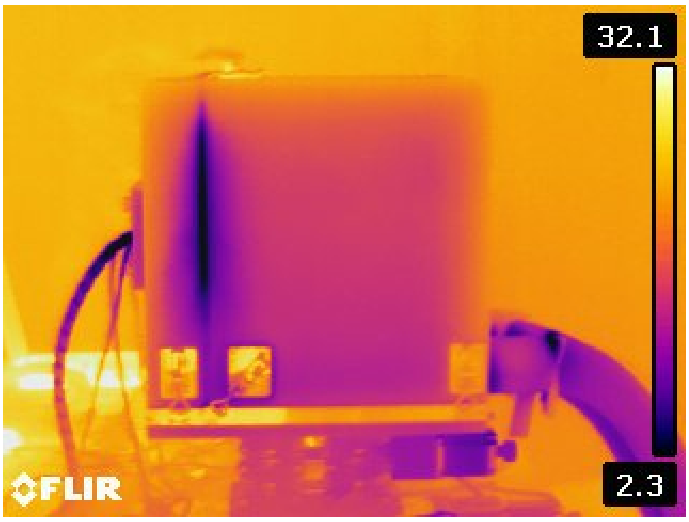

Figure 51: Infrared picture of the side of the box.

Image sources

[2] CERN. URL: https://cds.cern.ch/record/1621583/files/CERN's-accelerator-complex2013.jpg?subformat=icon-1440.

[4] CERN. URL: http://www.jetgoodson.net/content/images/thesis/theAtlasDetector.png.

[5] ATLAS Collaboration. URL: http://atlasexperiment.org/photos/atlas_photos/selected-photos/inner-detector/combined/0803014_01-A4-at-144-dpi.jpg.

[13] INSPIRE HEP. URL: https://inspirehep.net/record/1240499/files/LARG3-TDR-barrelM_samplings_presamp_new.png.

[17] ATLAS Collaboration. URL: http://atlasexperiment.org/photos/atlas_photos/selected-photos/muon-chambers/combined/0803017_01-A4-at-144-dpi.jpg.

[20] INSPIRE HEP. URL: https://inspirehep.net/record/1184943/files/IBL_figure1.png.

[22] Georgia State University. URL: http://hyperphysics.phy-astr.gsu.edu/hbase/solids/imgsol/band2.gif.

[23] Los Angeles University of California. URL: http://c125.chem.ucla.edu/BandGap.html.

[25] Wikimedia. URL: http://upload.wikimedia.org/wikipedia/commons/f/fa/Pn-junction-equilibrium-graphs.png.

[30] INSPIRE HEP. URL: http://inspirehep.net/record/1332745/files/graphics_HVCMOS_sketch.png.

[32] IPHC Strasbourg. *PICSEL Group*. 2015.

References

[1] I. Rubinskiy, EUDET Consortium, and AIDA Consortium. "An EUDET/AIDA Pixel Beam Telescope for Detector Development". In: *Physics Procedia* 37 (2012), pp. 923–931. DOI: 10.1016/j.phpro.2012.02.434.

[3] Oliver Sim Brüning et al. *LHC Design Report*. Geneva: CERN, 2004. URL: https://cds.cern.ch/record/782076.

[6] H. H. J. ten Kate. "ATLAS Superconducting Magnet System Status". In: *IEEE Transactions on Applied Superconductivity* 17.2 (2007), pp. 1191–1196. ISSN: 1051-8223. DOI: 10.1109/TASC.2007.898888.

[7] *ATLAS magnet system: Technical Design Report, 1*. Technical Design Report ATLAS. Geneva: CERN, 1997. URL: https://cds.cern.ch/record/338080.

[8] B Aubert et al. "Performance of the {ATLAS} electromagnetic calorimeter end-cap module 0". In: *Nuclear Instruments and Methods in Physics Research Section A: Accelerators, Spectrometers, Detectors and Associated Equipment* 500.1–3 (2003). {NIMA} Vol 500, pp. 178 –201. ISSN: 0168-9002. DOI: http://dx.doi.org/10.1016/S0168-9002(03)00344-9. URL: http://www.sciencedirect.com/science/article/pii/S0168900203003449.

[9] *ATLAS liquid-argon calorimeter: Technical Design Report*. Technical Design Report ATLAS. Geneva: CERN, 1996. URL: https://cds.cern.ch/record/331061.

[10] B. Aubert et al. "Construction, assembly and tests of the ATLAS electromagnetic barrel calorimeter". In: *Nuclear Instruments and Methods in Physics Research Section A: Accelerators, Spectrometers, Detectors and Associated Equipment* 558 (2006), pp. 388–418. DOI: 10.1016/j.nima.2005.11.212. URL: http://hal.in2p3.fr/in2p3-00024894.

[11] Pavol Bartos. *Performance of the ATLAS hadronic Tile calorimeter*. Tech. rep. ATL-CAL-PROC-2016-001. Geneva: CERN, 2016. URL: http://cds.cern.ch/record/2211419.

[12] *ATLAS tile calorimeter: Technical Design Report*. Technical Design Report ATLAS. Geneva: CERN, 1996. URL: https://cds.cern.ch/record/331062.

[14] C. Patrignani et al. "Review of Particle Physics". In: *Chin. Phys.* C40.10 (2016), p. 100001. DOI: 10.1088/1674-1137/40/10/100001.

[15] S. Palestini. "The muon spectrometer of the ATLAS experiment". In: *Nucl. Phys. Proc. Suppl.* 125 (2003). [,337(2003)], pp. 337–345. DOI: 10.1016/S0920-5632(03)91013-9.

[16] *ATLAS muon spectrometer: Technical Design Report*. Technical Design Report ATLAS. Geneva: CERN, 1997. URL: https://cds.cern.ch/record/331068.

[18] M Capeans et al. *ATLAS Insertable B-Layer Technical Design Report*. Tech. rep. CERN-LHCC-2010-013. ATLAS-TDR-19. 2010. URL: https://cds.cern.ch/record/1291633.

[19] J Albert et al. "Prototype ATLAS IBL Modules using the FE-I4A Front-End Readout Chip". In: *JINST* 7 (2012), P11010. DOI: 10.1088/1748-0221/7/11/P11010. arXiv:1209.1906 [physics.ins-det].

[21] G.F. Knoll. *Radiation Detection and Measurement*. Wiley, 2000. ISBN: 9780471073383. URL: https://books.google.ch/books?id=HKBVAAAAMAAJ.

[24] N. D. Arora, J. R. Hauser, and D. J. Roulston. "Electron and hole mobilities in silicon as a function of concentration and temperature". In: *IEEE Transactions on Electron Devices* 29.2 (1982), pp. 292–295. ISSN: 0018-9383. DOI: 10.1109/T-ED.1982.20698.

[26] R.F. Pierret. *Semiconductor Device Fundamentals*. Addison-Wesley, 1996. ISBN: 9780131784598. URL: https://books.google.ch/books?id=GMZFHwAACAAJ.

[27] N. Dinu. "Instrumentation on silicon detectors: from properties characterization to applications". Habilitation à diriger des recherches. Université Paris Sud - Paris XI, Oct. 2013. URL: https://tel.archives-ouvertes.fr/tel-00872318.

[28] I. Peric, C. Kreidl, and P. Fischer. "Particle pixel detectors in high-voltage CMOS technology-New achievements". In: *Nuclear Instruments and Methods in Physics Research Section A: Accelerators, Spectrometers, Detectors and Associated Equipment* 650.1 (2011). International Workshop on Semiconductor Pixel Detectors for Particles and Imaging 2010, pp. 158–162. ISSN: 0168-9002. DOI: 10.1016/j.nima.2010.11.090.

[29] B. RISTIC. "The FE-I4 telescope and HVCMOS measurements". 2014.

[31] M. GOFFE. "PICSEL Group: Physics with Integrated Cmos Sensors and ELectron machines". 2015.

[33] M. Benoit et al. "The FE-I4 Telescope for particle tracking in testbeam experiments". In: *JINST* 11.07 (2016), P07003. DOI: 10.1088/1748-0221/11/07/P07003. arXiv:1603.07776 [physics.ins-det].

[34] GORISEK A. and MCGOLDRICK G. "Synchronized analysis of testbeam data with the Judith software". 2013.

[35] Garrin McGoldrick, Matevz Cerv, and Andrej Gorisek. "Synchronized analysis of testbeam data with the Judith software". In: *Nuclear Instruments and Methods in Physics Research Section A: Accelerators, Spectrometers, Detectors and Associated Equipment* 765 (2014). HSTD-9 2013 - Proceedings of the 9th International "Hiroshima" Symposium on Development and Application of Semiconductor Tracking DetectorsInternational Conference Center, Hiroshima, Japan, 2 - 5 September 2013 ", issn = "0168-9002, pp. 140 –145. DOI: http://dx.doi.org/10.1016/j.nima.2014.05.033. URL: http://www.sciencedirect.com/science/article/pii/S016890021400552X.

[36] A. F. Zarnecki and P. Niezurawski. "EUDET Telescope Geometry and Resolution Studies". In: *ArXiv Physics e-prints* (Mar. 2007). eprint: physics/0703058.

[37] J. Idarraga M. Benoit and S. Arfaoui. "The AllPix Simulation Framework". 2016.

[38] *The Fundamentals of Modal Testing*. Tech. rep. 5954-7957E. USA: Agilent Technologies, 2000.

[39] BRINCKER R., VENTURA C., and ANDERSEN P. "Damping estimation by frequency domain decomposition". In: *Proceedings of the 19th International Modal Analysis Conference (IMAC)*. Kissimmee, Florida, 2001, pp. 698–703.

[40] L. HERMANS and H. VAN DER AUWERAER. "MODAL TESTING AND ANALYSIS OF STRUCTURES UNDER OPERATIONAL CONDITIONS: INDUSTRIAL APPLICATIONS". In: *Mechanical Systems and Signal Processing* 13.2 (1999), pp. 193 –216. ISSN: 0888-3270. DOI: http://dx.doi.org/10.1006/mssp.1998.1211. URL: http://www.sciencedirect.com/science/article/pii/S0888327098912110.